

**A Singular Vector ensemble
prediction system using the WRF
model**

Karimar Ledesma Maldonado

A thesis submitted in partial fulfillment of
the requirements for the degree of

Master of Science

Atmospheric and Oceanic Sciences

at the

UNIVERSITY OF WISCONSIN-MADISON

Spring 2022

Abstract

A Singular Vector ensemble prediction system using the WRF model

by Karimar Ledesma Maldonado

Uncertainties in both the initial conditions of a numerical weather prediction (NWP) model forecast and in the representation of the model dynamics evolve to contribute to forecast uncertainties. Because of these uncertainties, the day-to-day predictability of future atmospheric states remains a challenge. An ensemble of deterministic NWP model forecasts can be used to ascertain that predictability by providing information on the probability density function (PDF) of those future states or, at the least, the first two moments of the forecast state PDF, the forecast mean and the variance. In this project, singular vectors (SVs) are used to seed an ensemble forecast system. Singular vectors identify the initial locations and structures of growing perturbations that can contribute to ensemble spread and associated forecast uncertainty. This study evaluates a singular vector-based, Weather Research and Forecasting model (WRF) ensemble predictions system for short-range forecasting. This technique was tested for a given time interval (the optimization time) using a dry energy norm to identify a set of rapidly growing perturbations to a control forecast trajectory ordered by the growth rate, with the most rapidly growing SV called the “leading” SV. Further, a local projection operator (LPO) is employed to constrain optimization of perturbations over a selected area to compare with SVs estimated over the entire domain. Although results are case-dependent, both

experiments demonstrate a robust forecast spread for wintertime, mid-latitude weather systems.

Acknowledgements

I would like to express my sincere gratitude to the people that play an important role in my professional growth for the last three years and a half. First, I would like to thank my advisor Prof. Michael Morgan for his support, patience, motivation, guidance, immense knowledge and persistent help. Further I would like to thank Dr. Bret Hoover for his insightful comments and advice to this research. I would also like to thank the rest of my thesis committee Dr. Angela Rowe for their encouragement and support. It's has been an honor to work with all of them.

Besides of thesis committee members, I would like to thank UW-Madison faculty and staff for giving me the opportunity to complete a master's degree. I had met incredible and great scientists which I am being able to learn from them. To all of them, huge thanks for being patience and helping me to become the scientist I am today. In particular, I would like to thank to my mentor since 2012 Angel F. Adames Corraliza for his guidance and advice along the way.

Last but not the least, a huge thanks to my family Luis (Dad), Nilda (Mom), Armando (brother), Selimar (sister), Yamil (brother -in- law) and my beautiful niece Amalia for supporting me and holding my back every step of the way.

To all of you thank you in helping me to pursue my goals.

Contents

Abstract	i
Acknowledgements	iii
Contents	iv
List of Figures	vi
List of Tables	ix
Abbreviations	x
1 Introduction	1
1.1 Singular Vectors technique	4
1.2 Objectives	6
2 Mathematical formulation of Singular Vector	7
2.1 Requirements to compute Singular Vectors	13
3 Model, Data and Methodology	16
3.1 Weather Research Forecasting model	16
3.2 Data and experimental design	16
3.3 Construction of initial perturbations from SVs (Post Processing WRF SVs)	17
4 Synoptic Overview: Extratropical cyclone 4-5 December 2020	19
5 Results and Discussion	26
5.1 Total energy vertical profile	28
5.2 SV structure	30
5.3 Ensemble Prediction System	32
5.4 Short Range Ensemble Forecast (SREF) Plume Diagram	39
5.5 Estimate of Probability	43
6 Summary	58

List of Figures

1.1	A schematic of an initial condition-based ensemble. The black dot represent the control initial conditions and +, the perturb initial conditions. At initial time ($t=0$), the control and perturb initial conditions are slightly different starting conditions and after a short therm evolution ($t=$) the blue solid and dashed lines representing the control and perturb forecast, the envelope of perturbations deforms into an ellipse.	3
2.1	Representation of LPO in the model domain. LPO (black) grid points outside the region of interest (gray).	15
3.1	WRF domain setup for the entire domain (black) for EXP1 and LPO centered over the area of interest (blue) for EXP2.	18
4.1	250-hPa geopotential heights 1050 dam \pm 12 dam (green contours), temperature (red contours, interval 4°C), wind barbs (kt), and wind speed (kt, fill), (a)-(e) valid from 1200 UTC 4 December 2020 1200 UTC to 5 December 2020.	22
4.2	500-hPa geopotential heights 540 dam \pm 6 (green contours), temperature (red contours, interval 4°C), wind barbs(kt), and absolute vorticity ($\times 10^{-4}$ s $^{-1}$, fill), (a)-(e) valid from 1200 UTC 4 December 2020 to 1200 UTC 5 December 2020 1200UTC.	23
4.3	700-hPa geopotential heights 30d0m \pm 3 (dam, contour line), temperature (K, fill) and wind barbs (kt), (a)-(e), valid from 1200 UTC 4 December 2020 to 1200 UTC 5 December 2020.	24
4.4	Mean sea level pressure (hPa, contour lines) and 1000-to-500 hPa thickness (dam, green contours), (a)-(e) valid from 4 December 2020 1200 UTC to 5 December 2020 1200UTC.	25
5.1	WRF domain setup for the entire domain (black) for EXP1 and LPO centered over the area of interest (blue) for EXP2.	27
5.2	Singular values retrieved for EXP1 (left) and EXP2 (right).	28
5.3	Energy vertical profile at the (a) initial and (b) final time for EXP1. . . .	29
5.4	Energy vertical profile at the (a) initial and (b) final time for EXP2. . . .	29

5.5	500 hPa geopotential height (dam, black) and temperature field perturbation, (a) Initial and (b) final time corresponding to the first singular vector for EXP1. The line (B-A) denotes the extent of the vertical cross-section shown in Fig. 5.5a.	33
5.6	500 hPa geopotential heights (m, black), (a)-(b) zonal wind perturbations and (c)-(d) meridional winds perturbations at the initial and final time corresponding to the first singular vector for EXP1. The line indicates the region of the vertical cross-section shown in Figure-.	34
5.7	Cross section of temperature perturbations for (a) initial and (b) final time. Cross section orientations are shown in Figure 5.5 for EXP1.	35
5.8	Cross section of zonal wind perturbations for (a) initial and (b) final time. Cross section orientations are shown in Figure 5.6 for EXP1.	36
5.9	Cross section of meridional winds perturbations for (a) initial and (b) final time. Cross section orientations are shown in FFigure 5.6 for EXP1.	37
5.10	(a)-(c)The difference between the control forecast and the positive perturb forecast for temperature at 500 hPa at the initial and final time respectively for EXP1. (b)-(d) difference with respect negative perturb forecast.	38
5.11	500 hPa geopotential heights (m, black) and temperature field perturbation, (a) Initial and (b) final time corresponding to the first singular vector for EXP2.	39
5.12	500 hPa geopotential heights (m, black), (a)-(b) zonal wind perturbations and (c)-(d) meridional winds perturbations at the initial and final time corresponding to the first singular vector for EXP2.	40
5.13	(a)-(c)The difference between the control forecast and the positive perturb forecast for temperature at 500 hPa at the initial and final time respectively for EXP2. (b)-(d) difference with respect negative perturb forecast.	41
5.14	1004 hPa isobar for all ensemble members at the final time for (a) EXP1 and (b) EXP2. Control forecast (black line), mean (dashed black) positive perturb forecast (solid lines) and negative perturb forecast (dashed lines).	42
5.15	0°C isoline for all ensemble members, control forecast (black line), positive perturb forecast (solid lines) and negative perturb forecast (dashed lines) for (a) EXP1 and (b) EXP2.	43
5.16	Control forecast (solid), average (dashed), and perturb forecast (color-coded) for 0°C isoline at 850 hPa at the final time for (a) EXP1 and (b) EXP2.	44
5.17	Control forecast (solid), average (dashed), and standard deviation (shaded) for SLP at the final time for (a) EXP1 and (b) EXP2.	44
5.18	Control forecast (solid), average (dashed), and standard deviation (shaded) for temperature at 850 hPa at the final time for (a) EXP1 and (b) EXP2.	45
5.19	Average and standard deviation for total accumulated precipitation at the final time: (a)-(c) for EXP1 and (b)-(d) for EXP2.	46

5.20	Plume diagram, 2m Temperatures ($^{\circ}\text{C}$) from the WRF medium-range ensemble forecast system for EXP1 initialized at 1200 UTC 4 December 2020 for three different locations: (a) New York City, (b) Pittsburgh, and (c) Washington, D.C. Control forecast (bold black), perturb forecast (color-coded), ensemble mean (dashed black). The fields in panels (d)–(f) are repeated for EXP2.	48
5.21	Plume diagram, 10m wind speed (kt) from the WRF medium-range ensemble forecast system for EXP1 initialized at 1200 UTC 4 December 2020 for three different locations: (a) New York City, (b) Pittsburgh, and (c) Washington, D.C. Control forecast (bold black), perturb forecast (color-coded), ensemble mean (dashed black). The fields in panels (d)–(f) are repeated for EXP2.	49
5.22	Plume diagram, total accumulated precipitation (inches) from the WRF medium-range ensemble forecast system for EXP1 initialized at 1200 UTC 4 December 2020 for three different locations: (a) New York City, (b) Pittsburgh, and (c) Washington, D.C. Control forecast (bold black), perturb forecast (color-coded), ensemble mean (dashed black). The fields in panels (d)–(f) are repeated for EXP2.	50
5.23	The probability of occurrence of this event at each grid point which is computed by dividing the number of forecast members that predicted temperature below 0°C by the total number of forecasts, the total number of forecasts for (a) EXP1, (b) EXP2 and (c) EXP1-EXP2.	51
5.24	Forecasts of the estimated probability that SLP is below 1005 hPa during the 24h period beginning at 1200 UTC 4 December 2020 for EXP1. . . .	51
5.25	Forecasts of the estimated probability that SLP is below 1005 hPa during the period from 1200 UTC 4 Dec to 1200 UTC 5 Dec 2020 for EXP2. . .	52
5.26	The difference of probability of occurrence of this event at each grid point that predicted SLP is below 1005 hPa between EXP1 and EXP2.	53
5.27	Forecasts of the estimated probability for accumulation of liquid equivalent precipitation exceeding thresholds: (a) ≥ 0.1 inches, and (b) ≥ 0.5 inches at the final time 1200 UTC 5 December 2020 for EXP1.	54
5.28	Forecasts of the estimated probability for accumulation of liquid equivalent precipitation exceeding thresholds: (a) ≥ 0.1 inches and (b) ≥ 0.5 inches at the final time 1200 UTC 5 December 2020 for EXP2.	54
5.29	Forecasts of the estimated probability that wind speed at 10m is larger than 20kt during the period from 1200 UTC 4 Dec to 1200 UTC 5 Dec 2020 for EXP1.	55
5.30	Forecasts of the estimated probability that wind speed at 10m is larger than 20kt during the period from 1200 UTC 4 Dec to 1200 UTC 5 Dec 2020 for EXP2.	56
5.31	The difference of probability of occurrence of this event at each grid point that predicted wind speed at 10m is larger than 20 kt between EXP1 and EXP2.	57

List of Tables

5.1 Experiment Description	26
--------------------------------------	----

Abbreviations

SV	Singular V ector
NWP	Nnumerical W eather P rediction
WRF	W eather R esearch F orecasting model
TLM	Tangent L inear M odel
EPS	Ensemble P rediction S ystem
SREF	Short R ange E nsemble F orecast
OTI	Optimization T ime I nterval

Chapter 1

Introduction

The chaotic nature of the Earth system makes it challenging to predict future states of the system. Because numerical weather prediction models only approximate atmosphere dynamics and physical processes, there are uncertainties in numerical weather forecasts. In addition, initial condition uncertainties and errors can lead to lower predictability. These initial uncertainties and possible errors may be caused by the insufficiency of observations (or poor assimilation of the observations) in capturing important small-scale atmospheric features (Stensrud et al. (1999)) and affect predictability even for short-range forecasts (Lorenz (1963)). Model inaccuracies are likely to exist also, even as model grid spacing decreases (Heideman and Michael Fritsch (1988)). Hence, model and initial conditions uncertainties are not separable. Furthermore, the uncertainties and errors of a numerical weather forecast are flow dependent - they vary with each forecast cycle. Thus it is desirable to have some measure of forecast uncertainty with each deterministic forecast. The

only feasible technique to obtain estimates of forecast uncertainties (or the probability density function p.d.f. of those uncertainties) are Monte-Carlo techniques that sample the p.d.f. at initial time and evolve the sampled initial states with the forecast model — or a perturbed version of the forecast model to account for model uncertainty (Leutbecher and Palmer (2008)). The sample is referred to as an ensemble with the individual elements called the ensemble members. An ensemble forecast may be created from combinations of differing model physics or dynamical cores and/or sampling of the initial state with perturbed initial conditions. This study focuses on the latter.

Figure 1.1 shows a schematic of an initial condition ensemble. The control forecast trajectory is indicated by the line connected by the two bold dots, while ensemble members start from the cloud of +’s surrounding the control initial condition at $t = 0$. This cloud of +’s represents the initial uncertainty. The forecast model maps the initial states to the final states. The initial (circular) cloud of uncertainty is ultimately mapped into an ellipse of uncertainty - demonstrating that some uncertainties may grow, while others decay. The strategy of choosing effective perturbations is central to a useful ensemble.

Many methods have been developed to construct initial perturbations to create an ensemble prediction system, including the breeding vector (BV), singular vector (SV), and ensemble Kalman filter approaches. The breeding vector (BV) approach obtains the growing dynamical instabilities of the analysis error (Toth and Kalnay (1993)). This technique is closely related to the Lyapunov vectors of a dynamical system (Kalnay et al. (2002)). The improved version of BV applies the Ensemble Transform (ET) technique

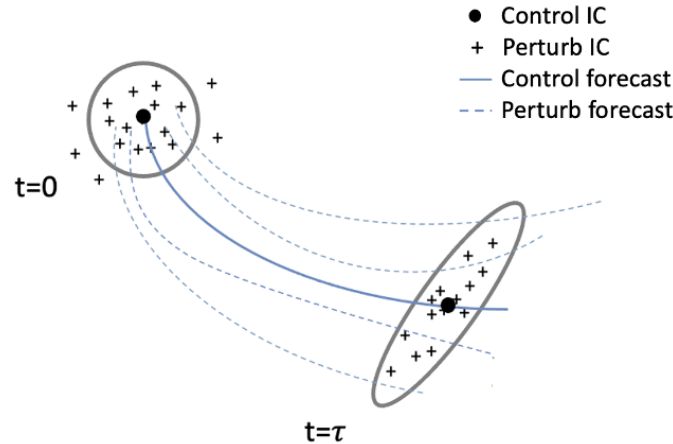


FIGURE 1.1: A schematic of an initial condition-based ensemble. The black dot represent the control initial conditions and +, the perturb initial conditions. At initial time ($t=0$), the control and perturb initial conditions are slightly different starting conditions and after a short term evolution ($t=$) the blue solid and dashed lines representing the control and perturb forecast, the envelope of perturbations deforms into an ellipse.

(Wei et al. (2008)). The Ensemble Transform breed vectors (ETBV) create globally orthogonal initial perturbations and is currently used to initialize the National Centers of Environmental Prediction (NCEP) global ensemble. Yet another technique is the singular vector (SV) method to identify the most rapidly growing perturbations over a prescribed optimization time interval (Lorenz (1965); Palmer (1993); Buizza et al. (1993); Molteni et al. (1996)). Forecast centers that use this technique to initialize ensemble forecasts include the European Centre for Medium-Range Weather Forecasts (ECMWF), Japan Meteorological Agency (JMA), Météo-France, and Bureau of Meteorology (BoM) in Australia. Another approach involves the use of the ensemble Kalman filter (Houtekamer et al. (1996), Houtekamer et al. (2005)); this technique uses an approximation of the Kalman filter equations. Observations are perturbed to generate a statistical sample of analyses. This approach is employed at the Meteorological Service of Canada and

Hungarian Meteorological Service. Another common approach to construct initial perturbations is the ensemble transform Kalman filter, in which perturbations are generated based on sampling the analysis uncertainties (Wei et al. (2006)). Previous studies have compared these different initial perturbation methods using different simplified models such as Lorenz, and atmospheric NWP models. (Anderson (1997); Trevisan and Legnani (1995); Houtekamer and Derome (1995); Trevisan et al. 2001; Wei and Frederiksen (2004); Bowler (2006); Wei et al. (2006); Descamps and Talagrand (2007); Yang et al. (2015); Zhou et al. (2016)). The SV technique has been often used for global ensembles such as that ECMWF system (Palmer et al. (1998a), Leutbecher (2005)). This study focuses on applying the SV technique to create an ensemble prediction system using a high-resolution **regional model**, which differs from prior work with SVs that is almost exclusively in lower-resolution global models.

1.1 Singular Vectors technique

SVs were first introduced by Lorenz (1965) in his attempt to determine the forecast error growth in a dynamic system and developed later by Lacarra and Talagrand (1988). SVs can be determined by solving an eigenvalue problem in which the solution provides a set of orthogonal eigenvectors. For a dynamical system, SVs describe a set of initial condition perturbations which amplify most rapidly over a prescribed time interval subject to the constraint of an initial time amplitude. Singular vectors can be used to construct an orthogonal hierarchy of most rapidly growing perturbations. The evolved leading SV will provide the direction in the phase space with a maximum growth (or amplification) that

produces the most extensive forecast spread. Hence, SVs aid in identifying the direction of initial uncertainty that produces the most significant forecast and model uncertainty. Since the optimization problem reduces to an eigenvalue problem, the Lanczos algorithm is an effective tool to compute the leading SV's with the desired accuracy (Parlett (1980)). This routine is coupled to the forward and adjoint linear models, then by a series of iterations, the largest eigenvalues and corresponding eigenvectors are found. Although it simplified to a linear problem, previous studies (Errico et al. (1993); Buizza and Palmer (1995), Errico and Raeder (1999); Hersbach (2000); Beare et al. (2003)) have shown that it still captures the dynamical evolution of fast-growing structures. To capture the dynamically most unstable perturbations it is necessary to define a norm at both initial and final times. The structure of SVs depends not only on the norm selected over a finite interval of time but also on how it is designed to focus on a particular forecast aspect. A complete discussion about the application of the norm is presented in section 2. Numerous studies have applied this technique to study the predictability of atmospheric flows by estimating the growth of forecast errors and creating ensemble weather prediction (Lorenz (1965); Palmer et al. (1994); Ehrendorfer and Tribbia (1997); Gelaro et al. (1998); Hakim (2000); Descamps et al. (2007)), the instability properties of atmospheric and oceanic flows by providing normal modes (Farrell (1982); Farrell (1989)) and last to target observations to determine the regions that are dynamically sensitive to enhance initial conditions for model forecasting (Palmer et al. (1998b)). To advance the understanding of weather predictions and research application into operations, the feasibility of the Singular Vectors (SVs) technique to the Weather Research and Forecasting (WRF)

model to create initial condition perturbations for short-range range ensemble weather predictions is evaluated. The WRF model is a mesoscale numerical weather prediction (NWP) and atmospheric simulation system designed for both atmospheric research and operational forecasting applications (Skamarock et al. (2008)) to address the needs and close ties between those communities.

1.2 Objectives

The objectives of this work are the development of a SV solver using the WRF model, application of this solver to create an SV-based ensemble prediction system for the evaluation of flow-dependent forecast uncertainty, and development of post-processing tools to reveal measures of forecast uncertainty.

Chapter 2

Mathematical formulation of Singular Vector

In this section, we discuss in detail the mathematical foundations of SVs. The discussion is a synthesis of explanations found in Lacarra and Talagrand (1988), Buizza et al. (1993), Molteni and Palmer (1993), Kalnay (2003) and Leutbecher (2007).

A nonlinear model approximates the dynamics of the Earth's atmosphere by solving the system of nonlinear equations that govern the atmospheric flow. This nonlinear model (M) predicts future atmospheric states represented as a one-dimensional column vector, X , called the "state vector." The state vector is composed of all the dependent forecast variables carried by the model such as temperature, wind, water vapor, and pressure. The time evolution of the state vector can be expressed as:

$$\frac{d\mathbf{X}}{dt} = \mathbf{F}(\mathbf{X}), \mathbf{X} = \begin{bmatrix} \mathbf{X}_1 \\ \cdot \\ \cdot \\ \cdot \\ \mathbf{X}_n \end{bmatrix}, \mathbf{F} = \begin{bmatrix} \mathbf{F}_1 \\ \cdot \\ \cdot \\ \cdot \\ \mathbf{F}_n \end{bmatrix} \quad (1)$$

where $\mathbf{X} \in \mathbf{R}^N$ denotes an N-dimensional model state vector and $\mathbf{F} \in \mathbf{R}^N$ denotes the N-dimensional representation of the model dynamical and the physical processes. The solution to Eq (1) $\mathbf{X}(t)$, describes the NWP model which maps the state vector at the initial time $\mathbf{X}(t_0)$ to the state vector at some future forecast time, t : $\mathbf{X}(t)$:

$$\mathbf{M} : \mathbf{R}^N \rightarrow \mathbf{R}^N \quad (2)$$

$$\mathbf{X}(t_0) \rightarrow \mathbf{X}(t)$$

$$\mathbf{X}(t) = \mathbf{M}(\mathbf{X}(t_0)) \quad (3)$$

The growth of small perturbations, x , of a numerical weather prediction model is approximated by solving a set of linear equations that govern the dynamics of the atmosphere obtained through a first-order Taylor expansion of the nonlinear model Eq (4) in where for short-time periods, the term $O(x^2(t))$ can be neglected. This system of linear equations

describe the dynamical evolution of perturbations linearized about a basic state control trajectory that is the output of (3).

$$\frac{d}{dt}(\mathbf{X}(t) + x(t)) = \mathbf{F}(\mathbf{X}(t) + x(t)) = F(\mathbf{X}(t)) + \left. \frac{\partial \mathbf{F}}{\partial \mathbf{X}} \right|_{x(t)} x(t) + O(x^2(t)) \quad (4)$$

The Eq (5) is the result of the subtraction of Eq (4) from Eq (1) and retaining the leading term. Equation (5) is the linearized model equation with Eq (6) the linearization of Eq (3) lead to defining the tangent linear model equation in Eq (7).

$$\frac{dx}{dt} = \left. \frac{\partial \mathbf{F}}{\partial \mathbf{X}} \right|_{\mathbf{X}(t)} x = \mathbf{A}_F x \quad (5)$$

where \mathbf{A}_F is the Jacobian of $\mathbf{F} : (\mathbf{A}_F)_{jk} = \frac{\partial \mathbf{F}_j}{\partial \mathbf{X}_k}$ a

$$x(t) = \left. \frac{\partial \mathbf{M}}{\partial \mathbf{X}} \right|_{X(t)} x(t_0) = \mathbf{L}(t_0, t)x(t_0) \quad (6)$$

where $\mathbf{L}(t_0, t) = \left. \frac{\partial \mathbf{M}}{\partial \mathbf{X}} \right|_{X(t)}$

$$x'(t) = \mathbf{L}(t_0, t)x'(t_0) \quad (7)$$

First, the input to the tangent linear model \mathbf{L} is the perturbation at initial time $x'(t_0)$. Note that the $\mathbf{L}(t, t_0)$ operator integration depends on the nonlinear trajectory to provide the evolved perturbation $x'(t)$ from an initial perturbation $x'(t_0)$.

To find those perturbations that have maximized the growth over a finite interval of time, we proceed to find the SV of the operator \mathbf{L} which are the eigenvectors of $\mathbf{L}^T\mathbf{L}$.

$$\mathbf{L}\mathbf{L}^T\mathbf{u}_i = \sigma_i^2\mathbf{u}_i \quad (8)$$

$$\mathbf{L}^T\mathbf{L}\mathbf{v}_i = \sigma_i^2\mathbf{v}_i \quad (9)$$

where \mathbf{L}^T the transpose of \mathbf{L} is the adjoint. Then, the eigenvectors of $\mathbf{L}^T\mathbf{L}$ are the left $(\mathbf{u}_1, \mathbf{u}_2, \mathbf{u}_3 \dots \mathbf{u}_n)$ and right $(\mathbf{v}_1, \mathbf{v}_2, \mathbf{v}_3 \dots \mathbf{v}_n)$ singular vectors of \mathbf{L} and the eigenvalues of $\mathbf{L}^T\mathbf{L}$ are the squares of the singular values $(\sigma_1^2, \sigma_2^2, \sigma_3^2 \dots \sigma_n^2)$ of \mathbf{L} . The singular values represent the major axes of the ellipse, which point in the direction of maximum perturbation growth over a short period of time, τ (**Figure 1.1**).

The matrix representation of \mathbf{L} and \mathbf{L}^T corresponds to the tangent linear model and the adjoint model, respectively. Both are used to compute the directions at initial time that evolve into the leading eigenvectors. The input variables for the adjoint model are the initial value of the trajectory $\mathbf{x}'(t_0)$ and the adjoint perturbation at final time.

Note that the dimension of this state vector \mathbf{X} is so large that it would be impractical to be store the propagator in matrix form. As a consequence, the coded tangent linear model and the adjoint model are used to identify the leading singular vectors via an iterative solution of an eigenvalue problem. The Lanczos algorithm iteration involves

an integration of the tangent-linear model and integration of the adjoint model over the optimization interval to reveal the SV and find the next largest SV.

The magnitude of the initial and final time perturbation require specification of a norm, E . In this study, the norm selected is energy and is discussed in detail in the next section.

We shall refer to $\|\bullet\|_E$ as the \mathbf{E} -norm, where the norms \mathbf{E} is Hermitian positive definite at the initial and final time respectively.

$$\|x'\|_{\mathbf{E}}^2 = \langle x, \mathbf{E}x \rangle = x\mathbf{E}x \quad (10)$$

The perturbation with the norm at the initial time is E_0

$$\|x'_0\|_{\mathbf{E}_0}^2 = \langle x'_0, \mathbf{E}_0x'_0 \rangle = x_0'^T\mathbf{E}_0x'_0 \quad (11)$$

The magnitude of the evolved perturbation with the norm E_t is defined as:

$$\|x'_t\|_{\mathbf{E}_t}^2 = \langle x'_t, \mathbf{E}_tx'_t \rangle = x_t'^T\mathbf{E}_tx'_t \quad (12)$$

where $\mathbf{E}_t = \mathbf{E}_t^T$. The amplification factor, σ , is defined as the ratio of the norm at the final time to the norm at the initial time:

$$\sigma^2 = \frac{\langle x'_t, \mathbf{E}_tx'_t \rangle}{\langle x'_0, \mathbf{E}_0x'_0 \rangle} = \frac{\langle \mathbf{L}x'_0, \mathbf{E}_t\mathbf{L}x'_0 \rangle}{\langle x'_0, \mathbf{E}_0x'_0 \rangle} = \frac{\langle \mathbf{L}^T\mathbf{E}_t\mathbf{L}x'_0, x'_0 \rangle}{\langle x'_0, \mathbf{E}_0x'_0 \rangle} \quad (13)$$

The initial perturbation that maximizes this ratio in an interval of time is considered the

fastest growing perturbation and is subject to the constraints that the initial amplitude is one, to satisfy the eigenvalue problem.

$$\vartheta(x'_0) = \langle \mathbf{L}^T \mathbf{E}_t \mathbf{L} x'_0, x'_0 \rangle - \sigma^2 (\langle \mathbf{E} x'_0, x'_0 \rangle - 1) \quad (14)$$

To maximize the growth of a chosen norm over a finite time interval $(t - t_0)$, the solution simplifies to a generalized eigenvalue problem:

$$\frac{\partial \vartheta}{\partial x'_0} = \mathbf{L}^T \mathbf{E}_t \mathbf{L} x'_0 - \sigma^2 \mathbf{E}_0 x'_0 = 0 \quad (15)$$

$$\mathbf{L}^T \mathbf{E}_t \mathbf{L} x'_0 = \sigma^2 \mathbf{E}_0 x'_0 = \mathbf{L}^T \mathbf{E}_t^{1/2} \mathbf{E}_t^{1/2} \mathbf{L} x'_0 = \sigma^2 \mathbf{E}_0 x'_0 \quad (16)$$

When different norms are used at the initial and final times then Eq (17) is used (an equivalent expression to the Eq (8)). The eigenvectors of $\mathbf{L}^T \mathbf{L}$ and the initial singular vectors of \mathbf{L} which are the perturbations with maximized amplification factor in the finite interval of time.

$$\left(\mathbf{E}_0^{-1/2} \mathbf{L}^T \mathbf{E}_t^{1/2} \right) \left(\mathbf{E}_t^{1/2} \mathbf{L} \mathbf{E}_0^{-1/2} \right) \mathbf{v}_i(t_0) = \sigma_i^2 \mathbf{v}_i(t_0) \quad (17)$$

The initial-time SVs form an \mathbf{E}_0 -orthonormal basis in which the lead SVs correspond to the fastest growing structure. Note that the SV calculation requires the TLM (\mathbf{L}) and

the adjoint of the TLM, \mathbf{L}^T . The solution forms orthogonal sets of vectors at the initial time and at the final time. The eigenvalues are real given the symmetry of the problem:

$$\mathbf{L}^T \mathbf{E}_t \mathbf{L} x'_0 = \sigma^2 \mathbf{E}_0 x'_0 \quad (18)$$

2.1 Requirements to compute Singular Vectors

Singular vector features are dependent on the selection of the norm, local projector operator (LPO), and optimization time interval (OTI) (Gelaro et al. (1998)).

a. Defined Norm

The calculation of SVs depends on the norm selected. While a norm representing the analysis uncertainty would be desirable, calculation of a flow dependent analysis error covariance is costly and memory requirements to store it, prohibitive. Previous studies have shown that the total dry energy is an appropriate metric for computing SVs for the predictability problem (Palmer et al. (1998b), Molteni et al. (1996)) as it is a first order approximation to the analysis error covariance matrix metric. The dry total energy is used in this study since previous results have shown that moist total energy is very similar to dry total energy norm (Kim and Jung (2009)). This total dry energy norm is defined as:

$$\varepsilon = \int_{\sigma} \int_x \int_y \left\{ \frac{(u'^2 + v'^2)}{2} + \frac{1}{2} c_p \theta'^2 + \frac{\theta_r R}{2} \left(\frac{p'}{p_r} \right)^2 \right\} \left(\frac{\partial p}{\partial \sigma} \right) dx dy d\sigma \quad (19)$$

where the primes denote the perturbations quantities $\mathbf{u}', \mathbf{v}', \theta', \mathbf{p}'$ for the model state vector comprising horizontal winds, potential temperature and surface pressure. The constant R is the gas constant for dry air, c_p is the specific heat for dry air at constant pressure ($=1006 \text{ JK}^{-1}\text{kg}^{-1}$), θ_r is a reference temperature ($=300 \text{ K}$) and p_r is a reference value for pressure ($=1000 \text{ hPa}$). The first term on the right-hand side represents the kinetic energy, the second term the available potential energy and the third term surface pressure component.

b. Optimization time interval (OTI)

The optimization time interval (OTI) is an interval of time over which the initial perturbations maximize their growth. Komori and Kadowaki, 2010 examined the sensitivity of SV to different OTIs where they found that mid-latitudes structures need longer OTI to develop contrary to smaller-scale which develops faster, that require shorter OTI. In this study, the optimization growth is $\tau = 24$ hours and it is assumed that uncertainties continue growing beyond that time.

c. The Local Projector Operator (LPO)

A local projection operator (LPO) is used to constrain the geographical region in which SVs are computed (Buizza and Palmer (1995)). Practically it focuses the region in which evolved perturbation amplitude is calculated while allowing the user to focus on weather systems of interest. The LPO sets the state vector to have zero values on grid points outside the region of interest and maximizes the energy of the singular vector at the final

time in the specified local region Figure 2.1. Therefore, perturbations chosen to grow in a specific geographical domain can be computed by applying LPO after the linear integration. Therefore, the generalized eigenvalue problem is defined as:

$$\left(E_0^{-1/2} \mathbf{L}^T \mathbf{P}^T E_t^{1/2}\right) \left(E_t^{1/2} \mathbf{P} L E_0^{-1/2}\right) v_i(t_0) = \sigma_i^2 v_i(t_0) \quad (20)$$

where \mathbf{P} is the projection operator and \mathbf{P}^T is its adjoint. Note that the LPO is self-adjoint, i.e., $\mathbf{P} = \mathbf{P}^T$.

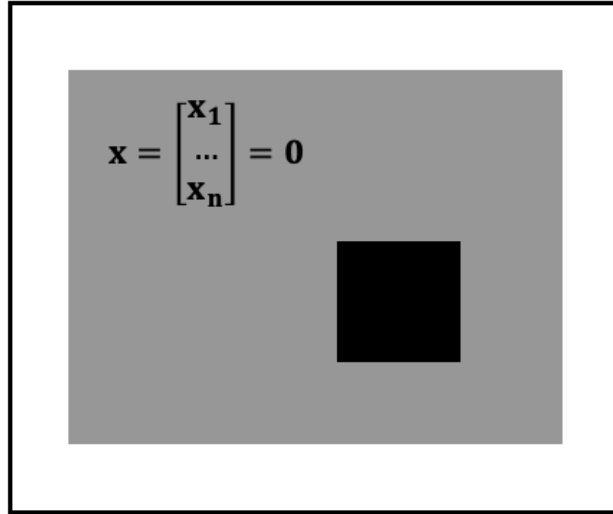


FIGURE 2.1: Representation of LPO in the model domain. LPO (black) grid points outside the region of interest (gray).

Chapter 3

Model, Data and Methodology

3.1 Weather Research Forecasting model

The Weather Research Forecasting (WRF) model is a nonlinear, non-hydrostatic, full-physics numerical weather prediction (NWP) model (Skamarock et al. (2008)) developed by the National Center for Atmospheric Research (NCAR), National Weather Service (NWS), and the academic community. In this study, WRF version 3.8.1 is used. This model has been widely used for a broad range of cases studies of extratropical and tropical weather systems. (Powers et al. (2017)).

3.2 Data and experimental design

The SVs are computed by solving an eigenvalue problem defined by the product of the tangent forward and adjoint operators and the dry total energy metric described in the

previous section. In this study, the initial and boundary conditions of the WRF simulations are taken from the Global Forecast System (GFS) analysis and forecast with a .25 degree resolution from the National Centers for Environmental Prediction (NCEP). Six-hourly analyses and their 3-h short term forecasts are used to provide the initial conditions and boundary condition updates for this study.

Previous studies have shown that SVs integrated with simplified physics in the linear model tend to survive the integration of the nonlinear dynamics and contribute to more considerable perturbation growth (Kim and Jung (2009), Barkmeijer and Palmer (1999)). Hence, the WRF TLM and adjoint model contain the moist physics scheme Thompson in this study. The nonlinear trajectory for the SV calculation is provided by a full-physics nonlinear integration of the forward model.

3.3 Construction of initial perturbations from SVs (Post Processing WRF SVs)

The SVs are used to construct the ensemble system by adding to and subtracting the initial conditions perturbations of u' , v' , θ' , μ' from the control forecast, and nonlinear integration is performed with the same initial time and a parent domain. Hence, the initial perturbations generated using the SVs are scaled as is shown in eq (21) and eq (22) to have the perturbation amplitude comparable to analysis error variance.

$$\mathbf{x}_0^+ = \mathbf{x}_0^{\text{ctl}} + \mathbf{v}'_n \alpha \frac{\sigma_1^2}{\sigma_n^2} \quad (21)$$

$$x_0^- = x_0^{\text{ctl}} - v'_n \alpha \frac{\sigma_1^2}{\sigma_n^2} \quad (22)$$

Where x_0^+ (x_0^-) is the positive (negative) perturbation, x_0^{ctl} is the control forecast, v'_n is the perturbation, σ_n^2 is the nth evolved SV and α an appropriate arbitrary scaling factor (= 50).

This approach allows us to show the range of possible outcomes and create the probability forecast for an event for a forecast variable such as temperature, wind, and precipitation. Therefore, the analysis for all experiments comprise $2N+1$ forecasts where one is the unperturbed member (the control forecast) and the other $2N$ are the perturbed analyses (Figure 3.1).

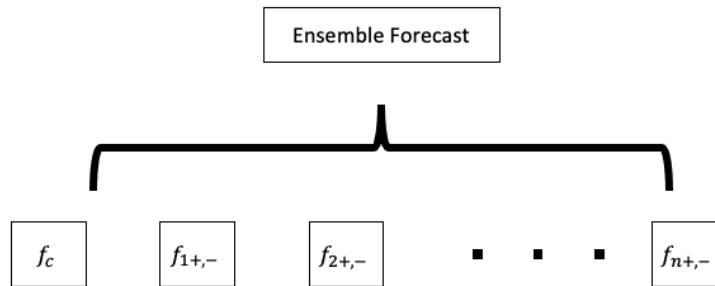


FIGURE 3.1: WRF domain setup for the entire domain (black) for EXP1 and LPO centered over the area of interest (blue) for EXP2.

Chapter 4

Synoptic Overview: Extratropical cyclone 4-5 December 2020

In order to evaluate the SV technique to identify forecast uncertainties we apply the technique to an east coast cyclogenesis event. The case chosen occur during the period 4-5 December 2020. The data used are the six-hourly NCEP GFS final analyses.

The synoptic overview begins at 1200 UTC on 4 December. Figure 4.1 displays the evolution of the 250 hPa geopotential height, wind, and isotachs. At 1200 UTC on 4 December (Figure 4.1a), a positively tilted shortwave trough, the precursor to the cyclogenesis event, is located over Missouri. A strong, 100 kt jet streak extends from northern Mexico to the southeast US coast to its south. The trough progresses eastward,

gradually becoming neutrally and then negatively tilted as it nears the east coast on 0600 UTC 5 December (Figure 4.1d).

In the mid-troposphere, a similar progression of events is seen (Figure 4.2) as the 500 hPa relative vorticity maximum associated with the short wave moves eastward and becomes more compact - a condition favorable for development at the surface. Concomitant with the relative vorticity amplifying are the 500 hPa geopotential height falls noted from 1800 UTC 4 December through 0000 UTC 5 December (Figure 4.2 b and c). As the shortwave energy moves through the slower moving, longer wavelength trough, its tilt shifts from positive to neutral (north-south) orientation on 0000 UTC 5 December 0000 UTC (Figure 4.2c) to a negative orientation (Figure 4.2e) by 1200 UTC on 5 December. This negatively-tilted trough observed at 1200 UTC on 5 December is associated with more substantial divergence, which would support stronger surface cyclogenesis.

Figure 4.3, shows the evolution of the 700 hPa geopotential height, temperature, and wind. The 700 hPa shortwave trough initially over Missouri (Figure 4.3a) moves eastward and becomes less positively tilted during the first 6 hours of the forecast (Figure 4.3b). The trough subsequently deepens and becomes negatively tilted as it approaches the East Coast (Figure 4.3 c, d, and e). As the 700 hPa short waves move eastward, a surface cyclone develops in the southeastern US (Figure 4.4c) and deepens as it moves northeastward. As low pressure occludes over the Appalachians, and eastern Great Lakes, southerly flow advects warm and moist air to the east coast, followed by a cold advection

on 5 December (Figure 4.2c) is observed moving over the Mid-Atlantic northward into the New England.

The evolution of the mean sea level pressure and 1000-to-500 hPa thickness (Figure 4.4) can discern the rapid development of this extratropical cyclone. At 1200 UTC on 4 December, could diagnose a broadly confluent, near-surface geostrophic wind field. The axis of dilatation of this confluent flow was oriented from southeast Louisiana to southern New England (Figure 4.4a). Over time, the near-surface temperature gradient intensified along the dilatation axis as a surface front developed (Figure 4.4 b and c). A surface cyclone formed along the front and progressed northeastward from the Carolinas (Figure 4.4c) to the mid-Atlantic coast by 1200 UTC on 5 December (Figure 4.4e). The cyclone began to deepen rapidly on 5 December at 0000 UTC, where the central pressure decreased by 24 hPa, in 12 hrs observed in Figure 4.4d and e.

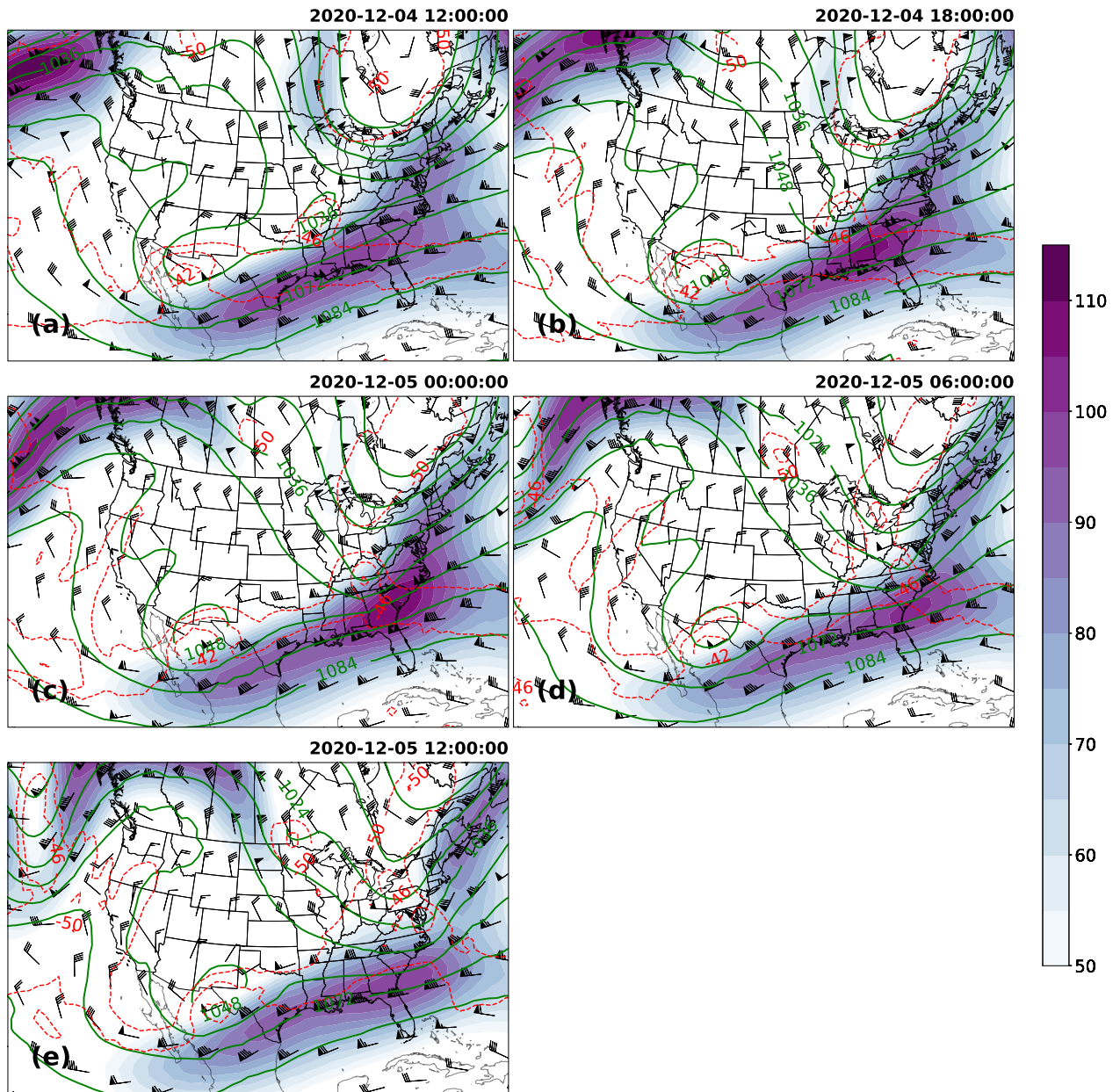


FIGURE 4.1: 250-hPa geopotential heights $1050\text{m} \pm 12$ (green contours), temperature (red contours, interval 4C), wind barbs (kt), and wind speed (kt, shaded), (a)-(e) valid from 1200 UTC 4 December 2020 1200 UTC to 5 December 2020.

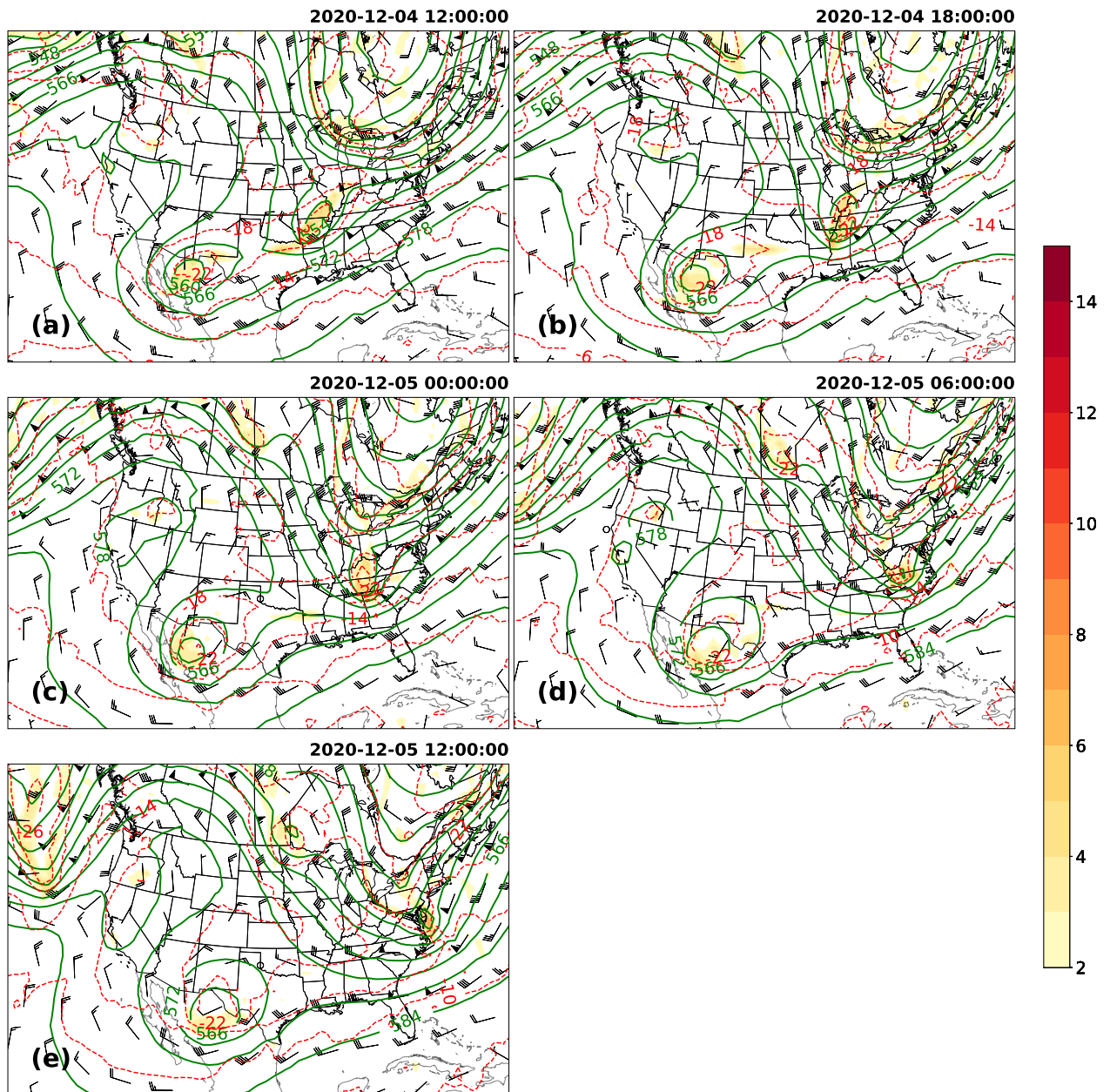


FIGURE 4.2: 500-hPa geopotential heights $540\text{m} \pm 6$ (green contours), temperature (red contours, interval 4°C), wind barbs(kt), and absolute vorticity ($\times 10^{-4} \text{ s}^{-1}$, shaded), (a)-(e) valid from 1200 UTC 4 December 2020 to 1200 UTC 5 December 2020 1200UTC.

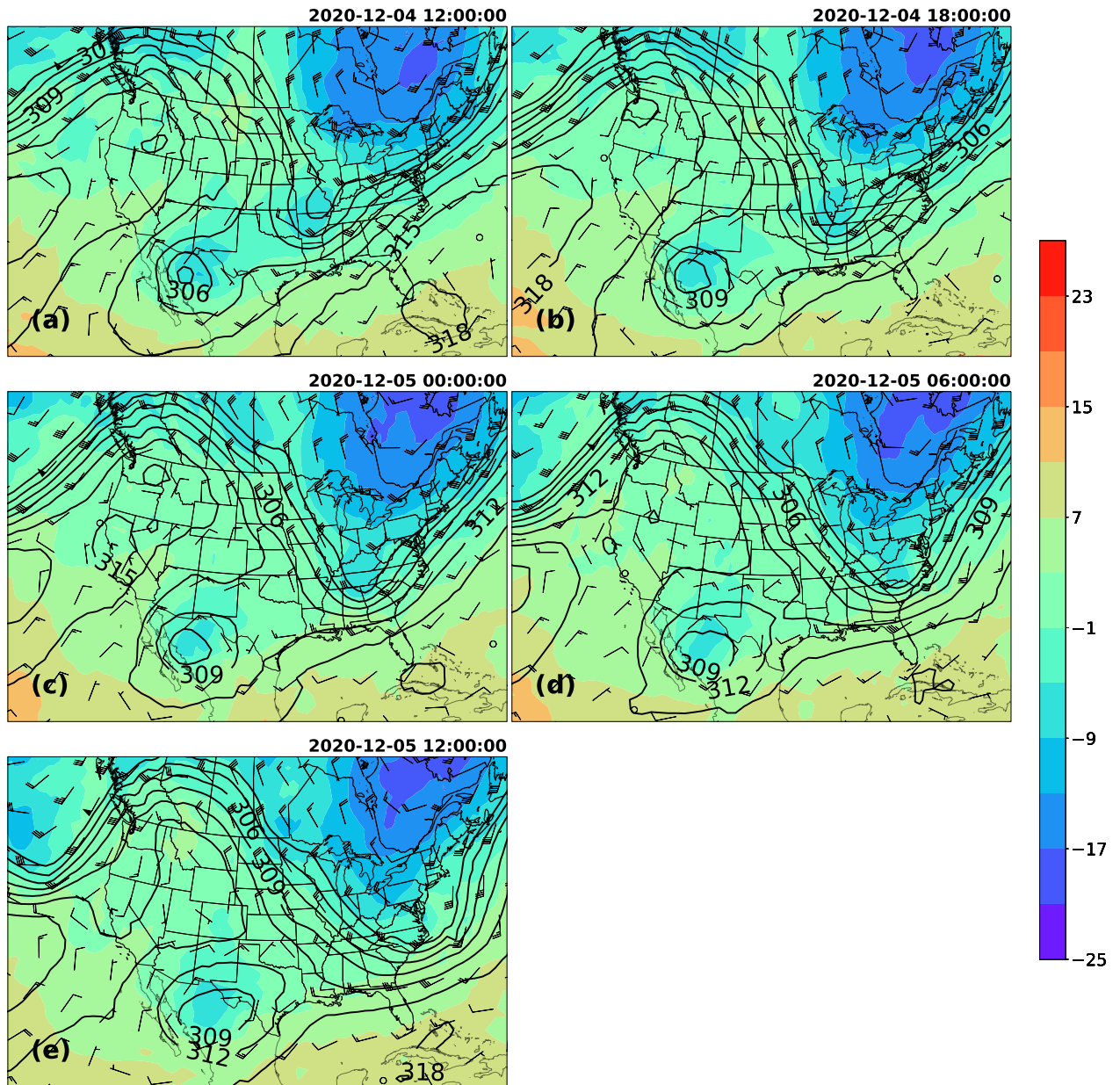


FIGURE 4.3: 700-hPa geopotential heights $300\text{m} \pm 3$ (m, contour line), temperature (K, fill) and wind barbs (kt), (a)-(e), valid from 1200 UTC 4 December 2020 to 1200 UTC 5 December 2020.

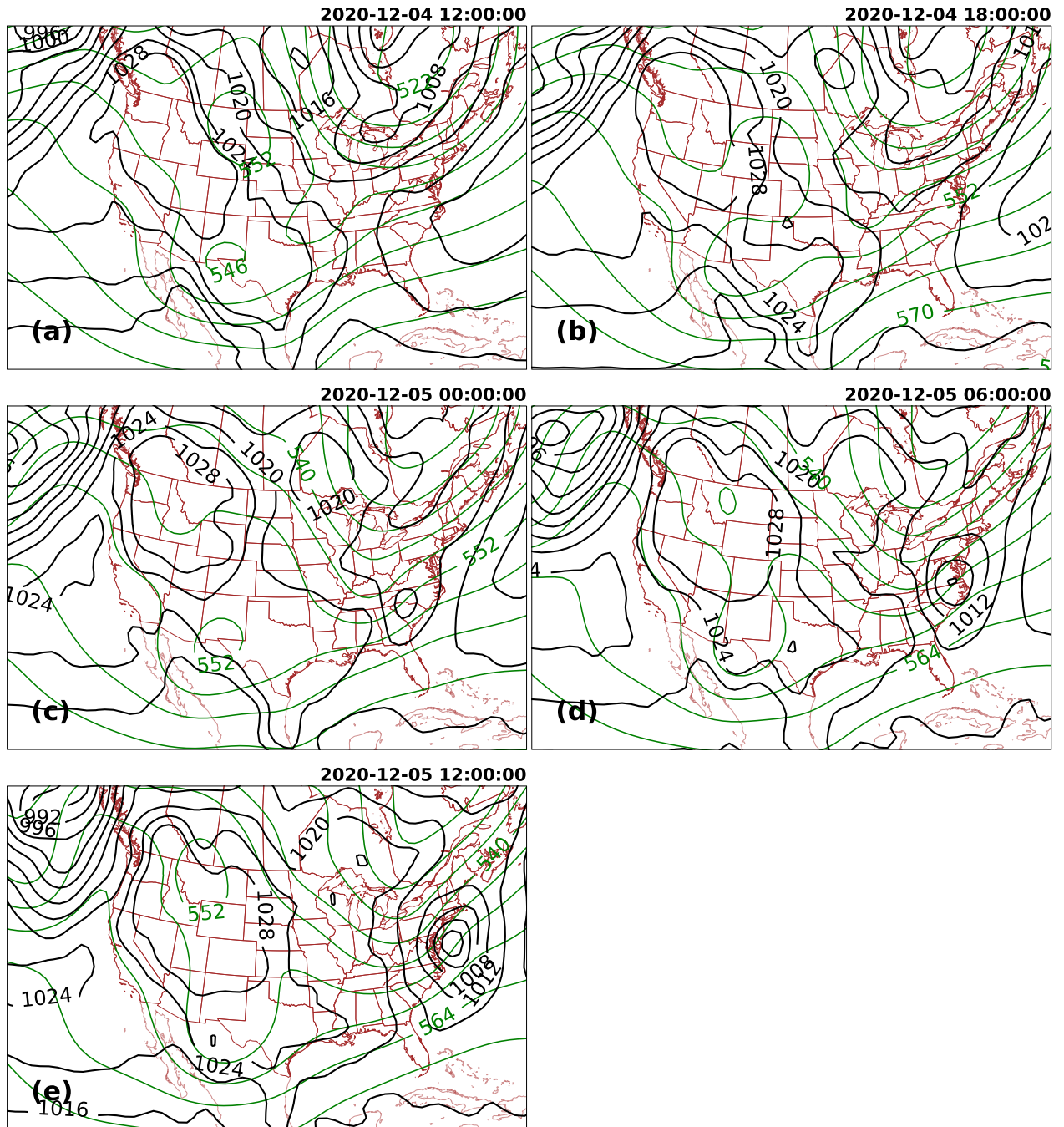


FIGURE 4.4: Mean sea level pressure (hPa, contour lines) and 1000-to-500 hPa thickness (dam, green contours), (a)-(e) valid from 4 December 2020 1200 UTC to 5 December 2020 1200UTC.

Chapter 5

Results and Discussion

In order to test the WRF SV system and the impact of the LPO on SV calculation, two sets of experiments were performed on the extratropical cyclone case described in the preceding chapter: (1) calculation of SVs over the entire domain (EXP1) and (2) another making use of an LPO situated over the development of the east coast storm (EXP2; see Figure 5.1). Table 5.1 summarizes the set of experiments. The SVs were calculated to maximize the 24h tropospheric total perturbation energy over the entire model domain (EXP1) and within the selected region identified by the LPO (EXP2).

	Experiment Description
EXP1	SV computed over the entire domain.
EXP2	computed with the LPO centered over the area of interest.

TABLE 5.1: Two sets of experiments. The integration and optimization time for all the experiments are 24 h.

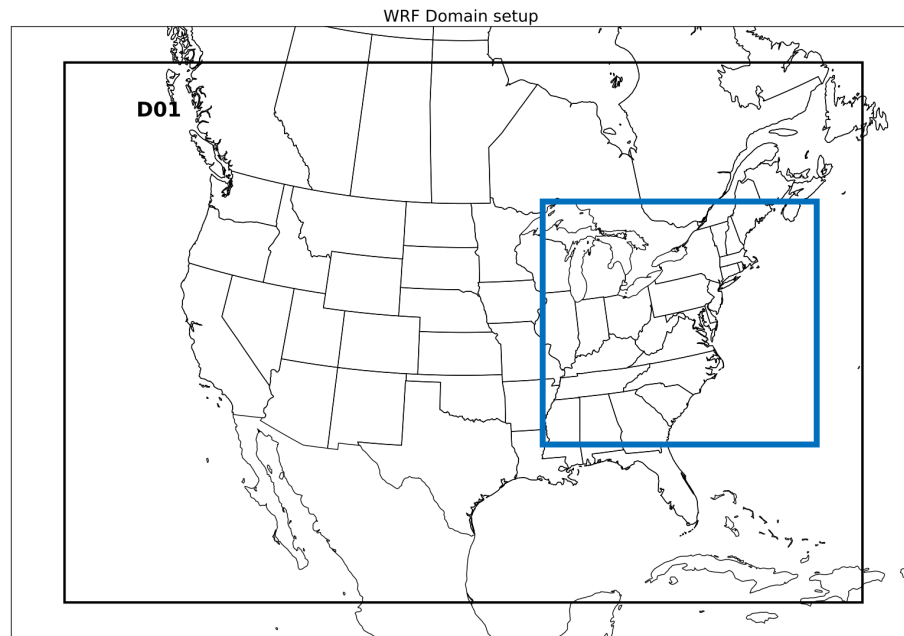


FIGURE 5.1: WRF domain setup for the entire domain (black) for EXP1 and LPO centered over the area of interest (blue) for EXP2.

All simulations were conducted on a 90 km, 78 x 48 grid with 41 evenly spaced vertical levels. The 24h numerical forecast for the control case was initialized at 1200 UTC 4 December 2020.

Figure 5.2 shows the distribution of the squares of the singular values retrieved following 100 iterations of the Lanczos algorithm for both experiments. For EXP1, 24 singular values were obtained, while for EXP2, 31 were retrieved. Recall that the squares of these values represent the ratio of the final time perturbation energy with a chosen domain (specified by an LPO) to initial time perturbation energy. Hence, the application of the local projection operator on EXP2 leads to smaller singular values compared with EXP1.

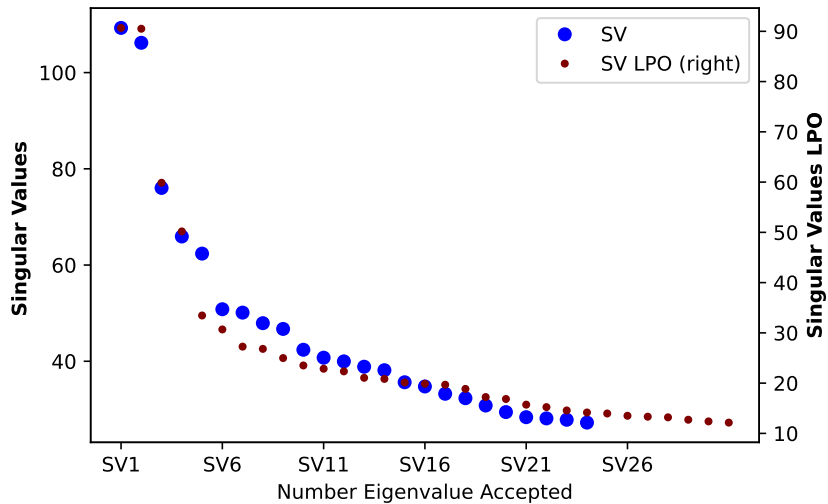


FIGURE 5.2: Singular values retrieved for EXP1 (left) and EXP2 (right).

5.1 Total energy vertical profile

The vertical profiles of the total perturbation energy for the first 10 (leading SVs) from EXP1 are displayed at the initial time (Figure 5.3a) and at the 24h optimization time (Figure 5.3b). Figure 5.4 shows the results for EXP2. Recall that the SV initial time total perturbation energy has been normalized to 1. The initial time SVs have the total perturbation energy maximized nearest the surface in both experiments. A secondary maximum is located in the model upper troposphere (particularly for SV1, SV9, and SV10 for EXP1 and SV6, SV7, SV9, and SV10 for EXP2). The evolved (final time) SVs experience an increase in energy at all levels, suggesting that at the initial time, the energy of SV is in the form of potential energy and that kinetic energy dominates the potential energy by the final time, as is shown in previous studies (Montani and Thorpe (2002)). Note that the surface-pressure term represents only a small portion of the total

energy.

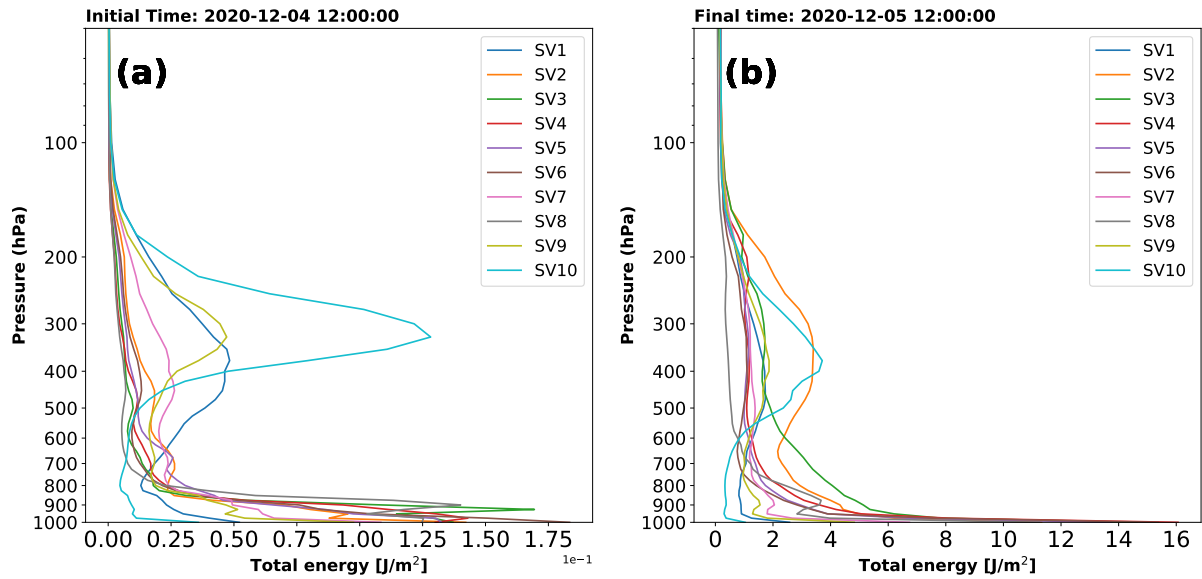


FIGURE 5.3: Energy vertical profile at the (a) initial and (b) final time for EXP1.

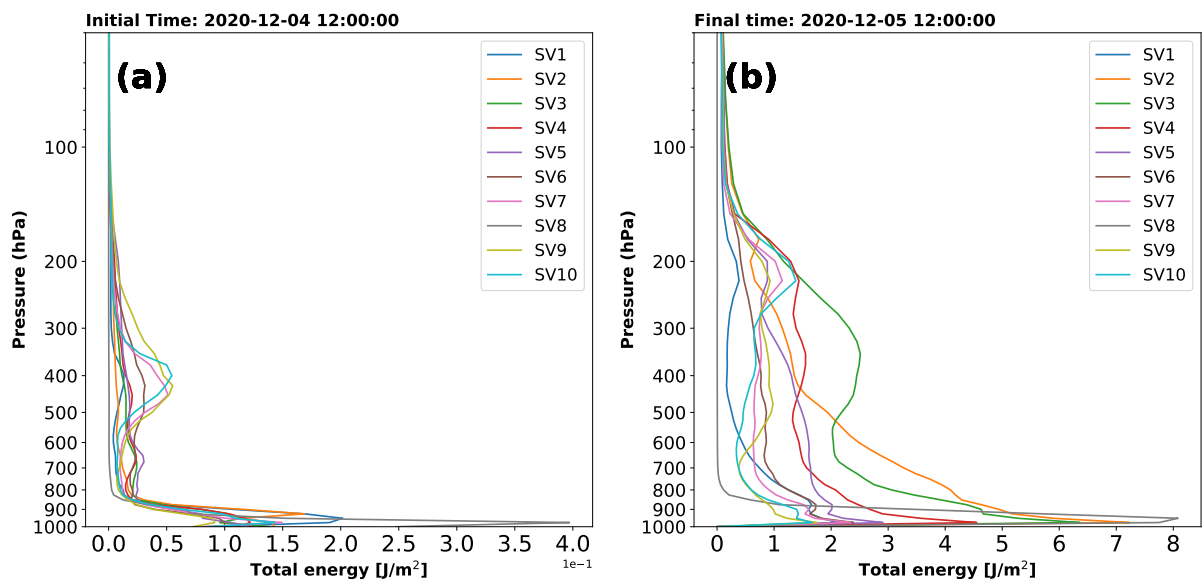


FIGURE 5.4: Energy vertical profile at the (a) initial and (b) final time for EXP2.

5.2 SV structure

A description of the initial and final structure of leading SVs for both experiments is presented in this section. The TLM is used to integrate the initial leading SV forward 24h. For the dry energy norm used here, the initial perturbation maximizes perturbation kinetic energy and available potential energy at the OTL.

The 500 hPa temperature perturbations associated with the leading SV exhibit a chevron-like pattern along the axis of the southwesterly jet is extending from northern Mexico into the southeast US (Figure 5.5a, Figure 5.11a). For EXP 1 (Figure 5.5a) the initial SV is maximized (at 500 hPa) over Texas and the western Gulf coast - well upstream of the final time cyclone position(Figure 5.5b). This structure is consistent with growing SVs having a horizontal tilt against the barotropic shear. In the 24 hr forecast, the perturbation grows in amplitude and broadens spatially (see Figure 5.5b, Figure 5.11b). While similar results were observed in EXP2 (Figure 5.11), the impact of the LPO on perturbation fields of EXP2 is evident, where the perturbation growth is restricted to the domain of the LPO. For example, the perturbation growth in the cut-off low over west Texas seen in (Figure 5.5)b is missing in the perturbation growth from (Figure 5.11)b.

An along the thermal wind shear vertical cross-section for θ , u , v is shown in Figure 5.7, Figure 5.8, Figure 5.9 respectively. The structure for the θ , u , v perturbations at the initial and final time illustrates an increase in amplitude and horizontal and vertical length scales as well as a change in tilt relative to the shear. For the variables analyzed,

at the initial time, the vertical upshear tilt (i.e., against the shear) is observed. The variables have maximum amplitude in the lower to middle troposphere as observed in prior idealized and real-world studies (Mukougawa and Ikeda (1994); Buizza and Palmer (1995); Hartmann et al. (1995); Hoskins et al. (2000)). There is also a wave train near the surface, which is evident in temperature and zonal and meridional winds. The horizontal temperature gradient (e.g., Figure 4.2a) associated with the vertical shear of the mean flow is the source of the available potential energy for growth. This westward tilt of the perturbations with height also implies that the horizontal temperature advection will increase the available potential energy, suggesting that vertical motion will convert perturbations of available potential energy to perturbations of kinetic energy experiencing transient growth. Badger and Hoskins (2000) showed that an up-shear tilted vertical structure contributes to kinetic energy growth and amplification of mid-latitude synoptic systems in baroclinically sheared flows. The increase in energy was also observed in the previous section 5.1. The positive correlation between temperature and meridional winds structure indicates the growth of baroclinic disturbances. The implied poleward heat transport is consistent with upward wave activity transport (Morgan (1999)). This vertical tilt pattern is a feature of SVs also observed in terms of potential vorticity (PV) (Montani and Thorpe (2002)). At the final time, the upshear tilt has largely disappeared and a longer horizontal wavelength is observed. In addition, an eastward tilt for temperature and almost vertical phase lines for zonal, meridional winds is also evident in EXP1 and EXP2 at the final time. Features responsible for the near-tropopause and near-surface energy maxima seen at the final time indicate baroclinically growing perturbations that favor

converting available potential energy into kinetic energy. Overall, SV structures tend to be concentrated upstream and in regions of maximum baroclinicity at the initial time and propagate through these regions and develop downstream waves at the final time. As explained in Chapter 2, SV structures depend on the norm selected. Both experiments were able to capture the SV growth and structure. Similar structures at the initial and final times were observed in EXP2.

Because perturbation growth is assumed to obey tangent linear dynamics, examining the differences between the nonlinear control and positively and negatively perturbed forecasts provides a means to evaluate this assumption. For both experiments, the difference between the control forecast and the positive (negative) perturb forecast at the 500 hPa temperature field at the initial and final time is shown in Figure 5.10a-c and Figure 5.13a-c) (Figure 5.10b-d and Figure 5.13b-d). The comparison between the control forecast and the perturbed forecast with the TLM output for this variable at this level shows a high degree of linearity because the perturbation fields appear to be "mirror" images of one another - particularly for EXP1. These results are consistent with previous studies in which nonlinearity for synoptic cases becomes important after two or three days (Errico and Raeder (1999); Buizza and Palmer (1995)).

5.3 Ensemble Prediction System

An ensemble prediction system (EPS) may elucidate the range of possible forecast outcomes. The ensemble presented here comprises 24 SVs, hence 49 individual forecasts

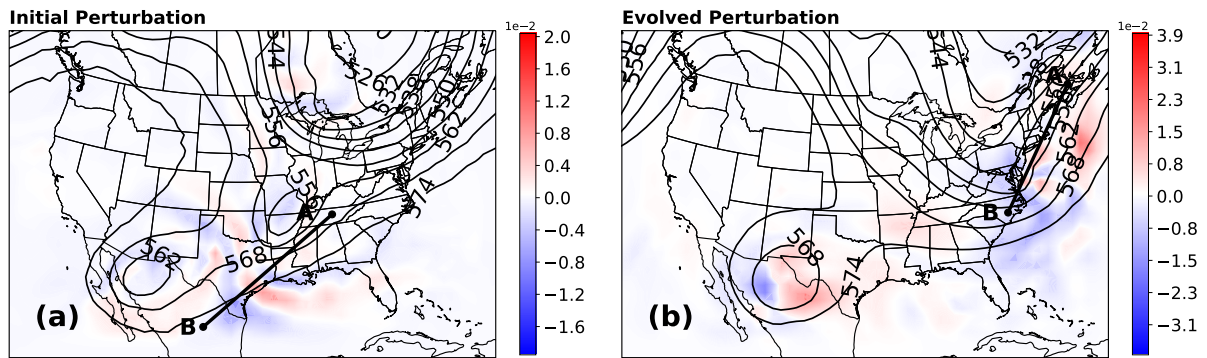


FIGURE 5.5: 500 hPa geopotential height (dam, black) and temperature field perturbation, (a) Initial and (b) final time corresponding to the first singular vector for EXP1. The line (B-A) denotes the extent of the vertical cross-section shown in Fig. 5.5a.

with 48 perturbed analyses and one unperturbed (control run). One means of displaying ensemble output is through the use of "spaghetti" diagrams which show the distribution of a particular contour of a given variable for each ensemble member. Figure 5.14 shows the 1004 hPa isobar (the lowest mean sea level pressure (MSLP) isobar observed) for both experiments at the final time. Each member is color-coded, the control forecast is bold black, and the mean is in dashed black. The areas in which large spread is observed offshore the mid-Atlantic coast are interpreted as high uncertainty in the control forecast for this variable.

Both experiments indicate a large spread in both the location and intensity of the surface cyclone (as measured by minimum MSLP). The large area enclosed by the 1004 hPa isobar of some ensemble members suggests a deeper cyclone and while the smaller area enclosed indicates weaker cyclones. In addition, the location of some ensemble members of the 1004 mb isobar is observed to the north (south), suggesting the forecast cyclone is propagating faster (slower) across ensemble members.

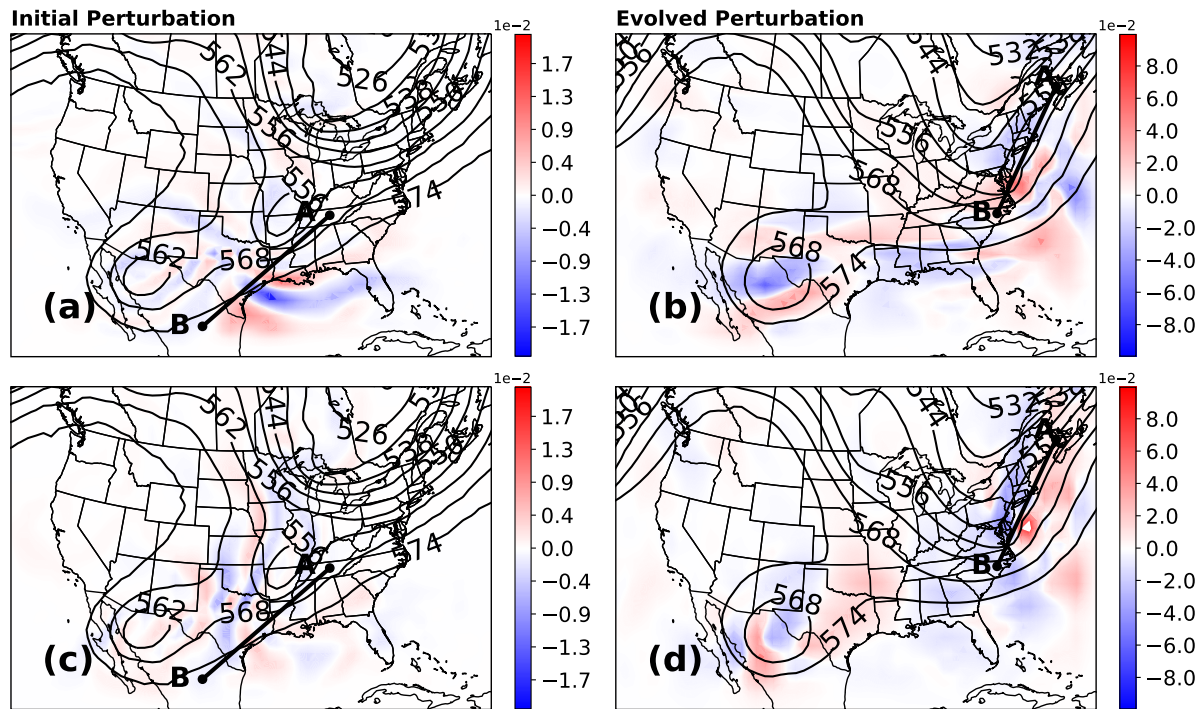


FIGURE 5.6: 500 hPa geopotential heights (m, black), (a)-(b) zonal wind perturbations and (c)-(d) meridional winds perturbations at the initial and final time corresponding to the first singular vector for EXP1. The line indicates the region of the vertical cross-section shown in Figure 5.8

From Figure 5.15, we can observe the forecast spread for the 0°C isotherm, where the region along the northeast coast shows the most significant spread. Comparing one isobar and the 0°C isotherm for some (random) ensemble members (Figure 5.16), from both cases, it suggests that the location and intensity of the cyclone along the east coast advect the isotherm further inland. In EXP1 (Figure 5.16a), we observed that for the blue ensemble member, the location of the minimum SLP is closer inland, and the isotherm advects to the east of Pennsylvania and northwest of Virginia. In contrast, the pink ensemble member seems to be more consistent with the control forecast. In EXP2, both ensemble members showed Figure 5.16b variation from the control forecast. The blue

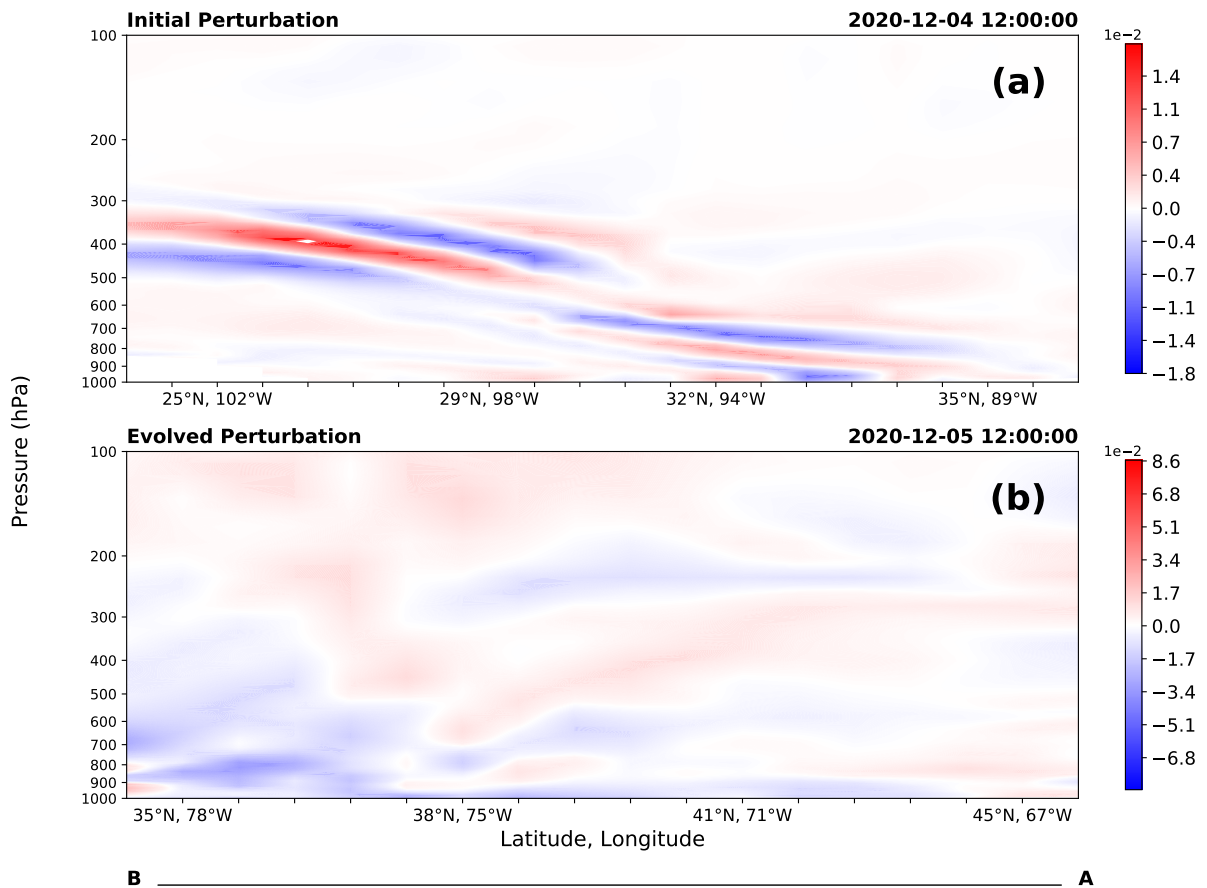


FIGURE 5.7: Cross section of zonal wind perturbations for (a) initial and (b) final time. Cross section orientations are shown in Figure 5.5 for EXP1.

ensemble location is further north and to the west, advecting the isotherm over the southern part of New York, New Hampshire, and west of Massachusetts. Meanwhile, the pink ensemble member, the SLP minimum is slight to the south, where the advection of the isotherm occurs to the east of Pennsylvania and the west of Maryland. The precipitation type falls in narrow bands (not more than 50 km wide); hence, the slightest temperature variations can mean the difference between rain, freezing rain, sleet, or snow. Therefore, this forecast output could help determine the precipitation type (i.e., snow, freezing rain, liquid water) that will likely occur and the possible areas affected. This is

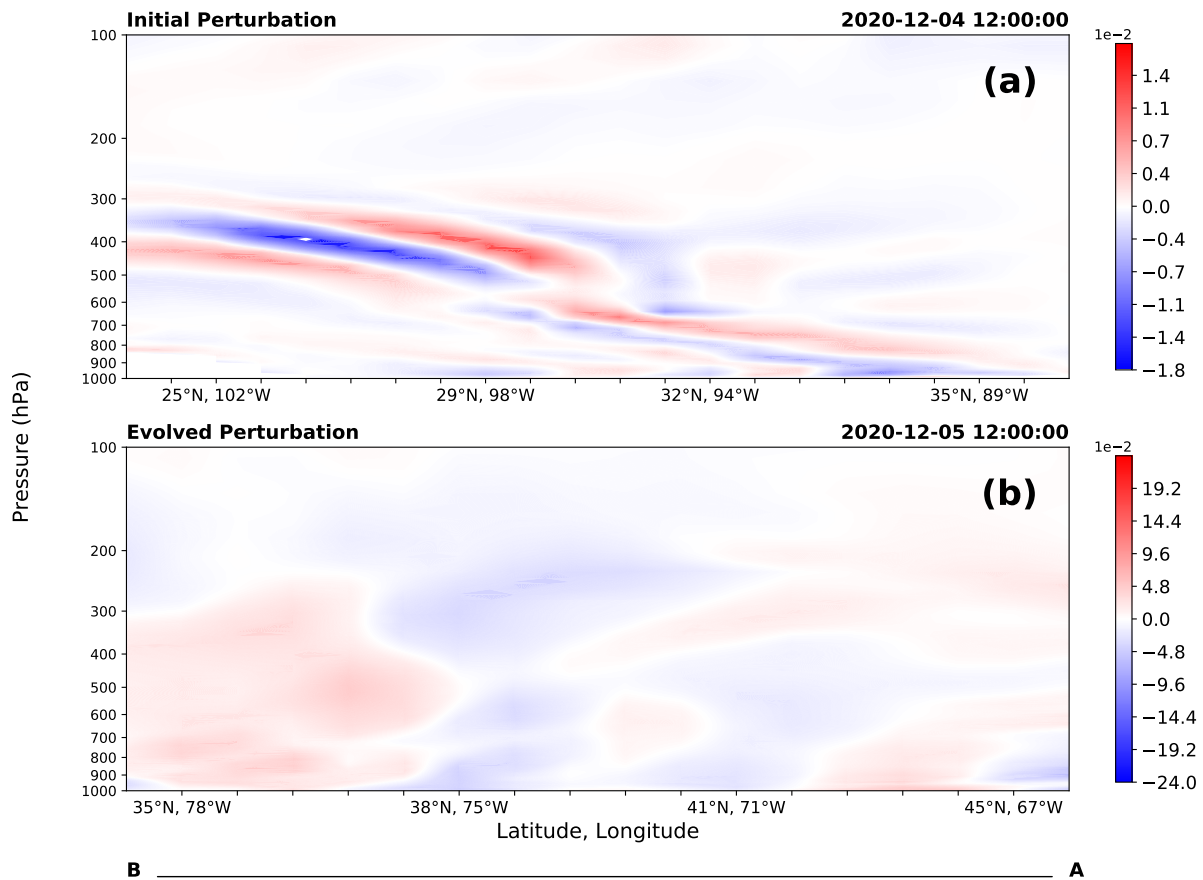


FIGURE 5.8: Cross section of zonal wind perturbations for (a) initial and (b) final time. Cross section orientations are shown in Figure 5.6 for EXP1.

in contrast to other areas where most ensemble members cluster together observed over Wisconsin, Illinois, and Kentucky, which would suggest greater confidence in the forecast of this variable.

Quantitatively, the spread is defined as the standard deviation of ensemble members from the ensemble mean. The spread among the forecasts at each grid point for mean sea level pressure, temperature, and the total accumulated precipitation increase along the northeast coast (see Figure 5.17), Figure 5.18, Figure 5.19) in both experiments.

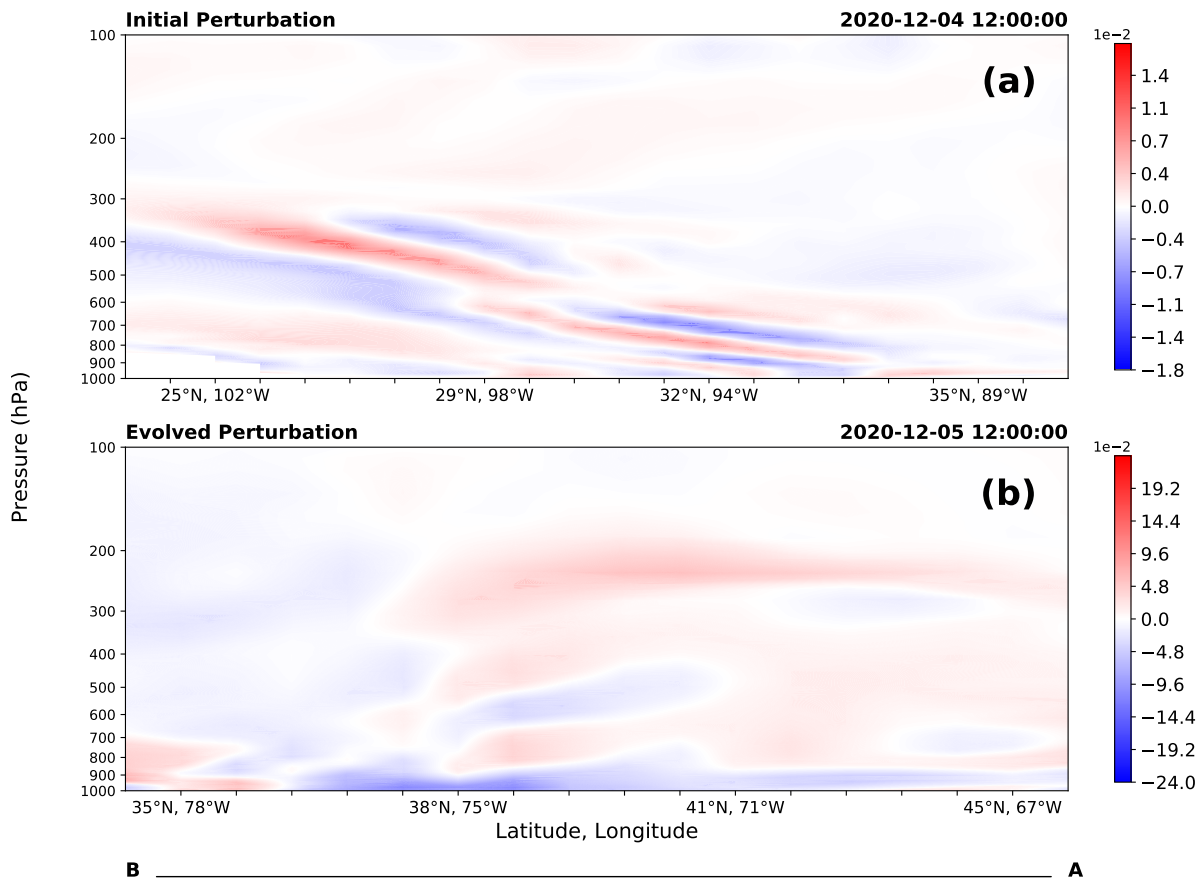


FIGURE 5.9: Cross section of meridional winds perturbations for (a) initial and (b) final time. Cross section orientations are shown in Figure 5.6 for EXP1.

These results demonstrate the ability of the ensemble to reveal the spread in the model variables associated with variations in the initial conditions. Note that when SVs are calculated over the entire domain, we observed variance over the whole domain as well, and this is consistent with all variables, while when the LPO is used, the variance is observed closer to the region selected by the LPO. Note that larger MSLP spread over northern Mexico in EXP1 compared with EXP2 (see Figure 5.17). However, although both experiments indicate a spread over the east coast of the US for the three variables analyzed here, a larger spread is observed in EXP2, because the LPO was used.

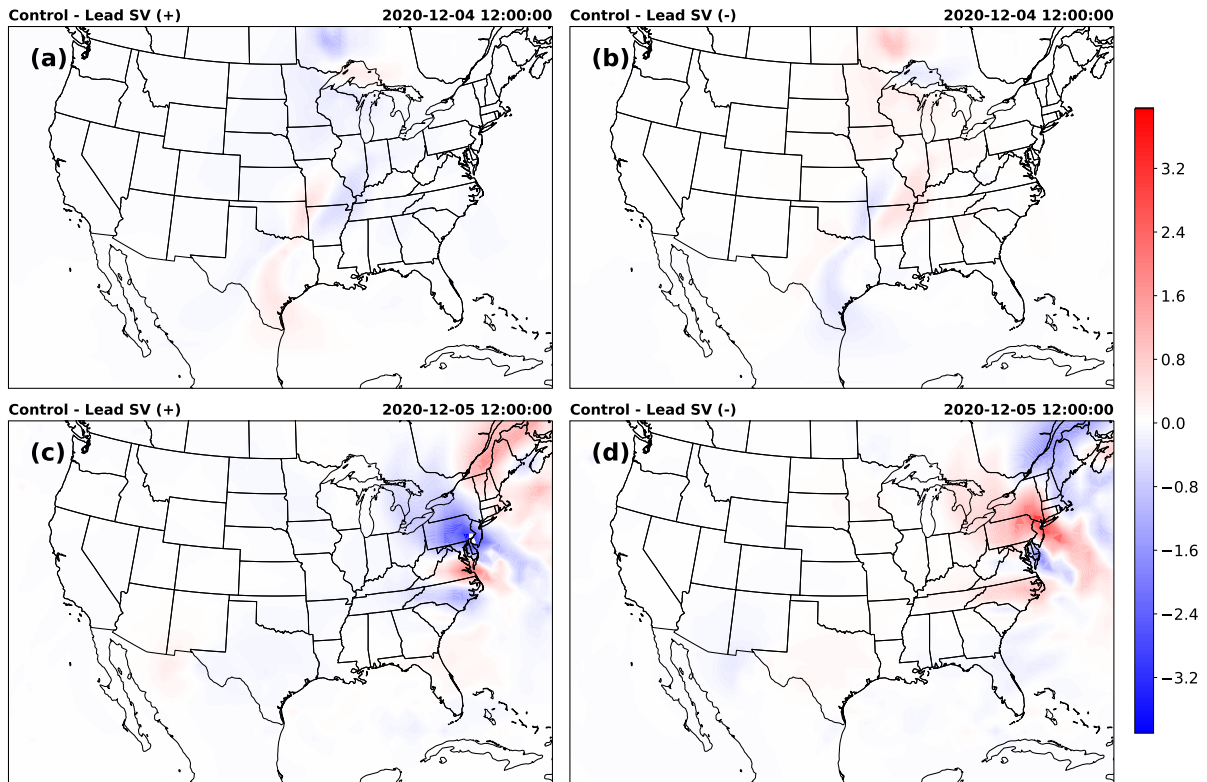


FIGURE 5.10: (a)-(c) The difference between the control forecast and the positive perturbation forecast for temperature at 500 hPa at the initial and final time respectively for EXP1. (b)-(d) difference with respect to negative perturbation forecast.

The variability in MSLP location and intensity will help determine the amount of air moisture that moves over land that can impact the temperature by advecting the 0°C isotherms (Figure 5.15, Figure 5.16) and produce more accumulated precipitation. Figure 5.18 illustrates the spread in temperature at 850 hPa for both experiments, where EXP2 shows a more significant variation in temperature over the east coast of the US. As a consequence, the total accumulated precipitation will vary over the region, as is observed in Figure 5.19. The accumulated precipitation variable only estimated the total liquid water content. Although the average total accumulation in precipitation in both experiments is consistent, comparing the standard deviation, the more extensive spread

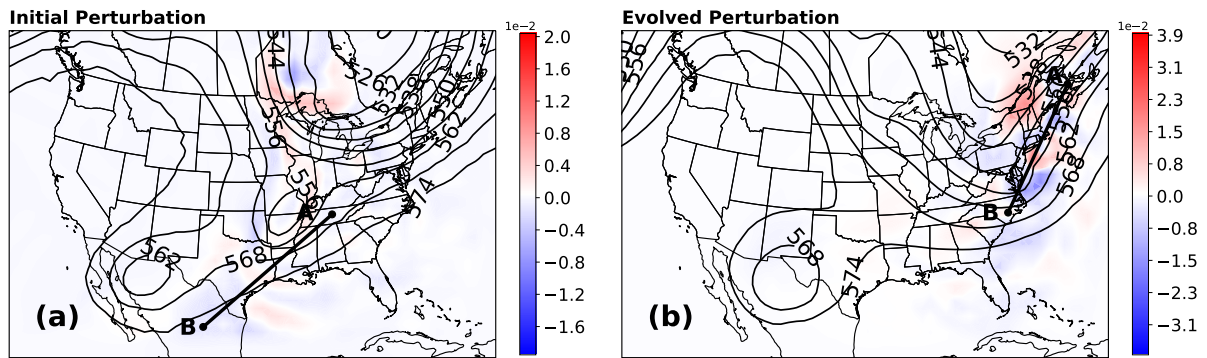


FIGURE 5.11: 500 hPa geopotential heights (m, black) and temperature field perturbation, (a) Initial and (b) final time corresponding to the first singular vector for EXP2.

is observed in EXP2 (Figure 5.19d), consistent with the previous variable. This result suggests that the use of the LPO can enhance the spread in variables not included in the energy norm.

5.4 Short Range Ensemble Forecast (SREF) Plume

Diagram

Short-range ensemble forecast products show the time evolution of a forecast variable for each ensemble member (48 perturbed members), the control forecast, and the ensemble mean from a grid point for different locations such as New York City (NYC; 40°N, 75°W), Pittsburgh (PIT; 40°N, 79°W), and Washington, D.C (DC; 39°N, 77°W). The output is available at 3h intervals through 24 hours. We can observe the cluster and the outliers in both experiments for variables such as 2m temperature, 10m wind speed, and total accumulated precipitation.

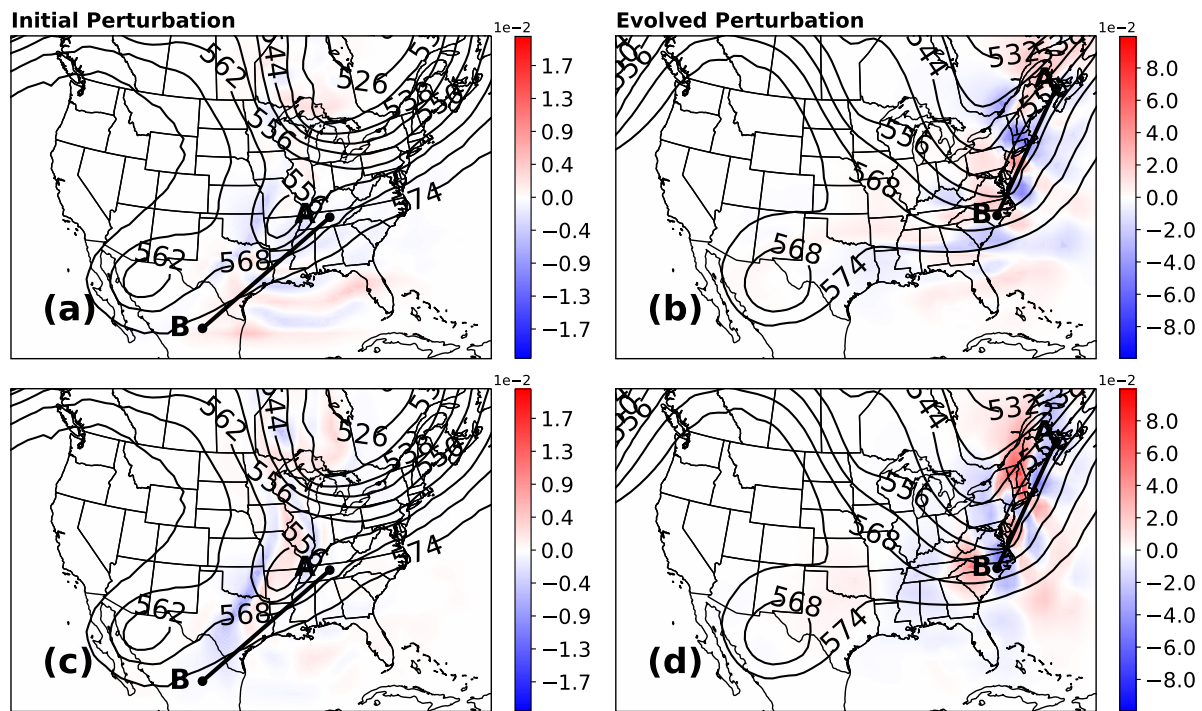


FIGURE 5.12: 500 hPa geopotential heights (m, black), (a)-(b) zonal wind perturbations and (c)-(d) meridional winds perturbations at the initial and final time corresponding to the first singular vector for EXP2.

Figure 5.20a-c (Figure 5.20d-f) displays the plume diagram for forecast 2-meter temperature for EXP1 (EXP2) at 3-hour intervals out to 24 hours. The warm outliers in the plume diagram correspond to an ensemble member with slower cold front progression. In contrast, the cold outliers have a rapid cold front passage for a given location. The decreasing temperatures during the day are consistent with increasing cold advection in the wake of the developing coastal cyclone. The location where more ensemble members tend to be above the mean and control forecast implies the larger tendency to have warmer temperatures by the final time, suggesting weaker cold advection in the wake of the surface cyclone. The spread in the EXP1 2-meter temperature forecast for PIT and

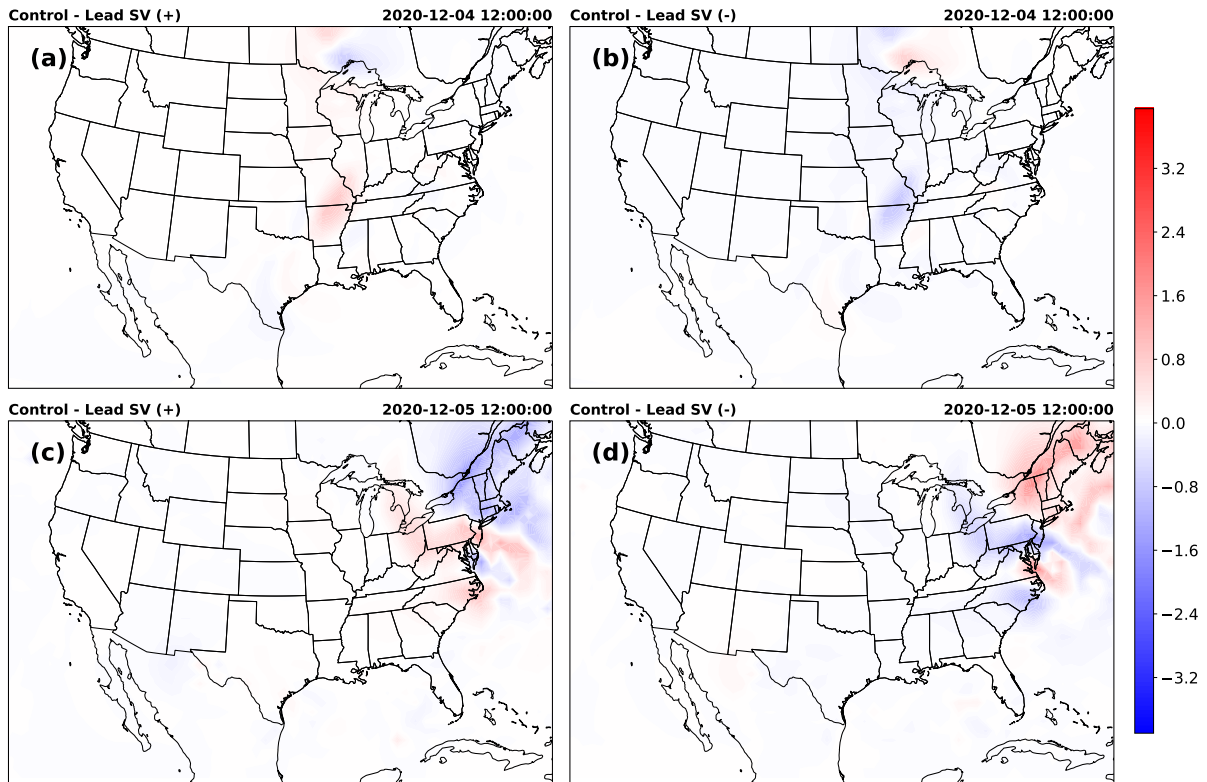


FIGURE 5.13: (a)-(c) The difference between the control forecast and the positive perturbation forecast for temperature at 500 hPa at the initial and final time respectively for EXP2. (b)-(d) difference with respect to negative perturbation forecast.

DC are relatively small until about 1200 to 1500 UTC, while in the first 3h of the forecast, the spread increases briefly in NYC. Interestingly, the spread for EXP2 near-surface temperature forecasts (Figure 5.20d-f) increases immediately for all three locations, with the largest spreads observed for NYC and PIT. The spread in the temperature among ensemble members increases to 5°C for EXP1 and 6°C at the final time. These results are consistent with what was observed in the preceding sections, where some ensemble members indicate faster (slower) displacement of the cyclone (i.e., Figure 5.16). In both experiments, the control forecast and the mean for the temperature at 2m seem consistent.

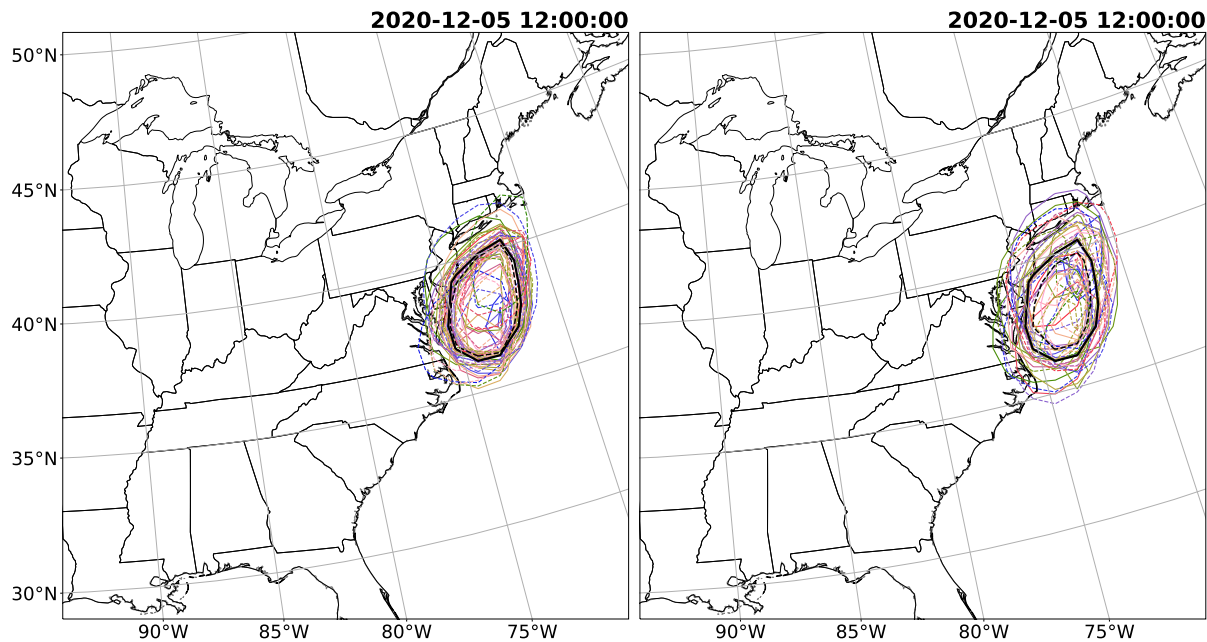


FIGURE 5.14: 1004 hPa isobar for all ensemble members at the final time for (a) EXP1 and (b) EXP2.. Control forecast (black line), mean (dashed black) positive perturb forecast (solid lines) and negative perturb forecast (dashed lines).

Figure 5.21a-c (Figure 5.21d-f) illustrates the forecast for 10-meter winds speed for EXP1 (EXP2). In both experiments, PIT shows the largest spread among the ensemble members after 3h; however, EXP2 shows a large spread among the ensemble members for the three locations. Further, based on those plume diagrams, we observed an overall increase in wind speed by the final time in NYC and DC, suggesting the passage of a cold front. Contrary to the temperature at 2m, the mean for the wind speed at 10m is below the control forecast, indicating that more ensemble members predict weaker winds.

A similar analysis for the total accumulated precipitation for both experiments is shown in the Figure 5.22a-c (Figure 5.22d-f). Both show an increase in the total accumulated precipitation starting around the same times at 1500 UTC for NYC, 0600 UTC for PIT, and

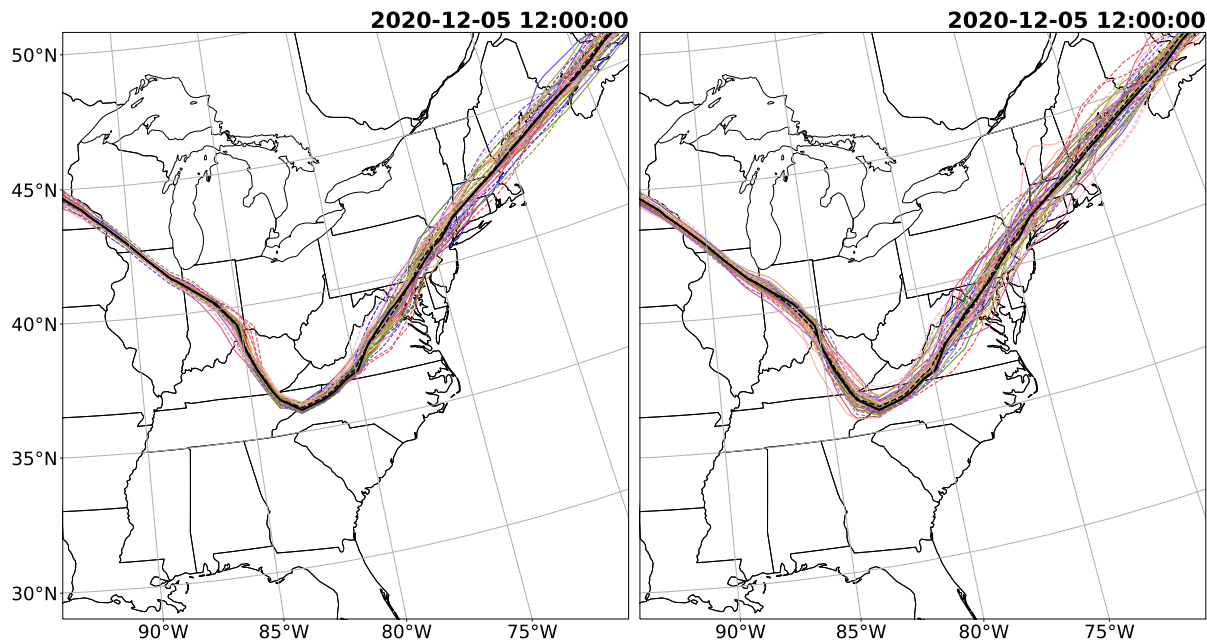


FIGURE 5.15: 0°C isoline for all ensemble members, control forecast (black line), positive perturb forecast (solid lines) and negative perturb forecast (dashed lines) for (a) EXP1 and (b) EXP2.

1200 UTC for DC, while EXP2 shows a slight increase in the spread in total accumulated precipitation by the final time in PIT and DC (Figure 5.22b and Figure 5.22f). The mean is slightly above the control run for the total accumulated precipitation, suggesting that the ensemble members tend to predict larger precipitation accumulation. Additionally, comparing both experiments, the plume diagram for EXP2 shows more spread among the ensemble members, particularly for the 2-m temperature.

5.5 Estimate of Probability

The EPS can assess the probability of exceeding forecast thresholds for temperature, mean sea level pressure, and precipitation.

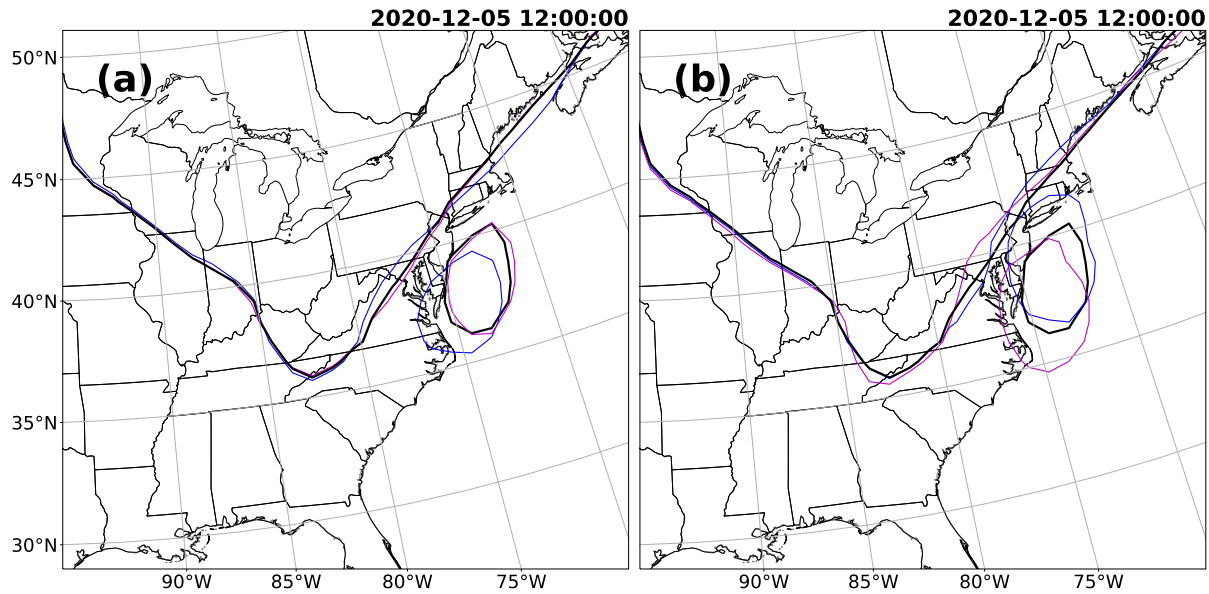


FIGURE 5.16: Control forecast (solid), average (dashed), and perturb forecast (color-coded) for 0°C isoline at 850 hPa at the final time for (a) EXP1 and (b) EXP2.

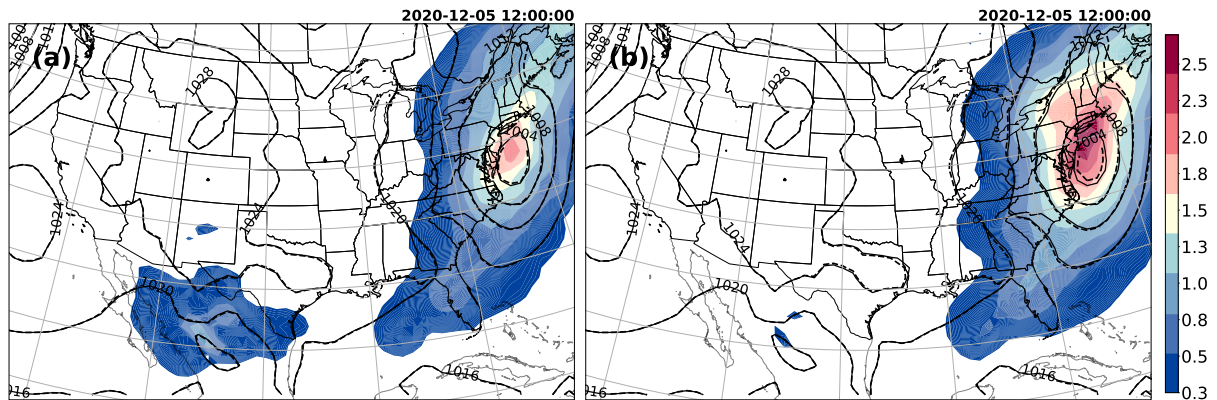


FIGURE 5.17: Control forecast (solid), average (dashed), and standard deviation (shaded) for SLP at the final time for (a) EXP1 and (b) EXP2.

Figure 5.23 illustrates a post-processing procedure to calculate the probability the predicted temperature falls below 0°C . For the event under consideration, this probability would be useful in assessing whether freezing precipitation or icy conditions were possible in the northeastern US. The estimated probabilities calculated at each grid point are the

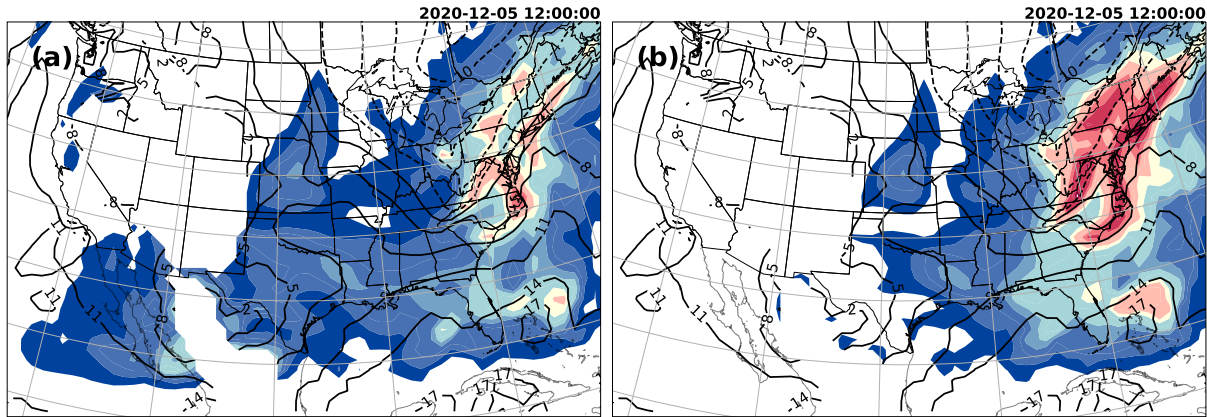


FIGURE 5.18: Control forecast (solid), average (dashed), and standard deviation (shaded) for temperature at 850 hPa at the final time for (a) EXP1 and (b) EXP2.

ratio of the number of ensemble members with a temperature at or below freezing to the total number of ensemble members. The total number of forecasts for EXP1, EXP2, and the differences between EXP1 and EXP2. Both experiments produce similar probabilities to predict temperature below 0°C (Figure 5.23a and Figure 5.23b). Observing the difference between both experiments, (Figure 5.23c) the blue areas identify regions that EXP1 is more likely (about around 12 % points higher) to predict temperature below 0°C while the red areas suggest that EXP2 is about 7% points higher in predicting a temperature below 0°C .

To estimate the probability that at each grid point the pressure is lower than 1005 hPa, the number of forecast members that predicted SLP below 1005 hPa is divided by the total number of ensemble members (49). In Figure 5.24 and Figure 5.25, the 6 hourly estimates of this probability is shown. The intensification of the cyclone in these six-hourly maps through the final time is evident. The probability of observing SLP below 1005 hPa increases from 10% at 0600 UTC (Figure 5.24d) to 95% at 1200 UTC (Figure 5.24e) in

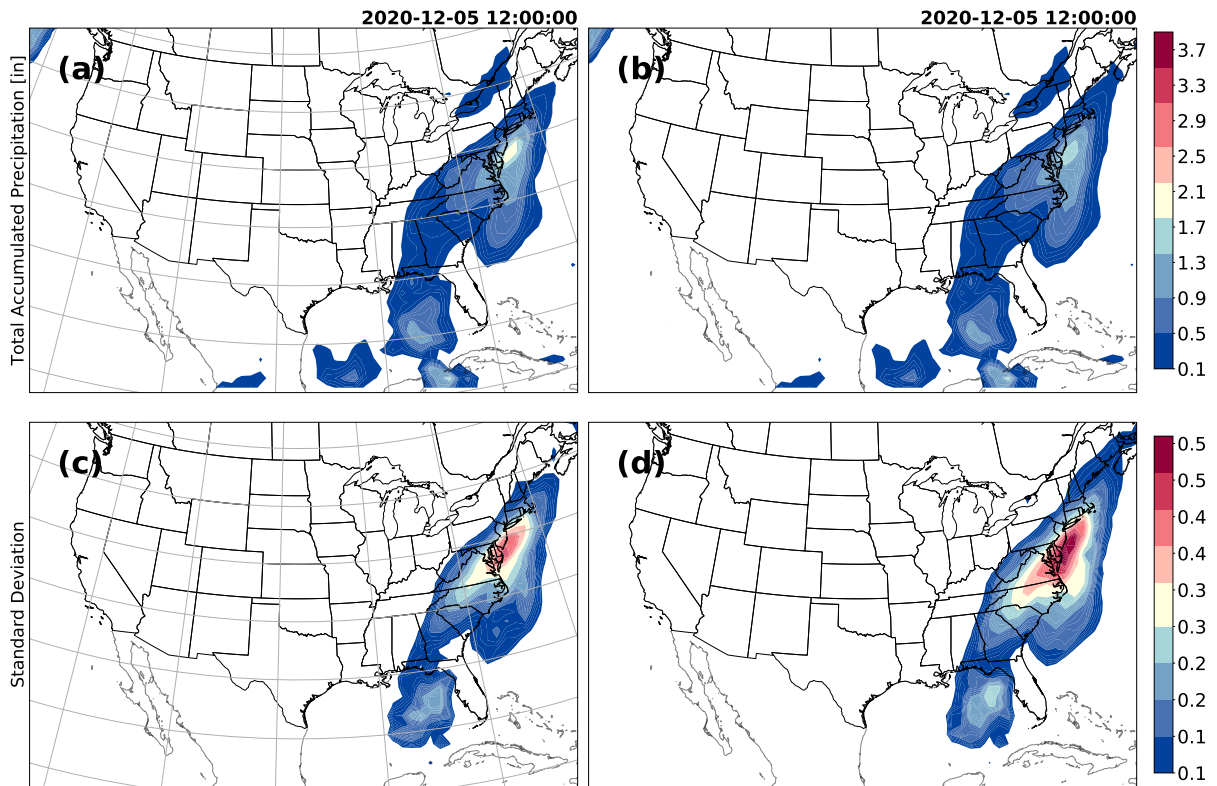


FIGURE 5.19: Average and standard deviation for total accumulated precipitation at the final time: (a)-(c) for EXP1 and (b)-(d) for EXP2.

EXP1, suggesting baroclinic influences that could contribute to faster development of the cyclone. This set of figures demonstrates the probability of intensification of extratropical cyclones. The 24h difference between EXP1 and EXP2 is shown in Figure 5.26;. However, both experiments suggest areas to predict SLP below 1005 (around 15%), and EXP1 (red areas) shows a more extensive distribution, suggesting a more intense development than EXP2.

Figure 5.27 and Figure 5.28 show the probability of occurrence of precipitation exceeding 0.01" (panel a) and 0.5" (panel b) for both experiments computed as the relative frequency of these events for both experiments, respectively. As would be expected, the results

suggest a slight decrease in area and probability by increasing the total accumulation threshold. While both sets of probability charts appear similar, the probabilities with EXP2 are somewhat lower for both thresholds. Given the earlier evidence for a slightly stronger cyclone in the EXP1, this may suggest the role of diabatic heating differences influencing the cyclone intensity (less for EXP2).

Figure 5.29 and Figure 5.30 show the probability of 10m wind speed exceeding 20kt. Both experiments show consistent results for the area and timing of increasing probability for wind speeds exceeding the 20kt threshold. It is important to point out that in Figure 5.29d and Figure 5.30d we observe a larger probability in EXP1, suggesting faster development. In Figure 5.31 we observe that 20 % (red areas) is more likely for wind speed at 10 m \geq 20 kt in EXP1, while 15 % (blue areas) is more likely in EXP2.

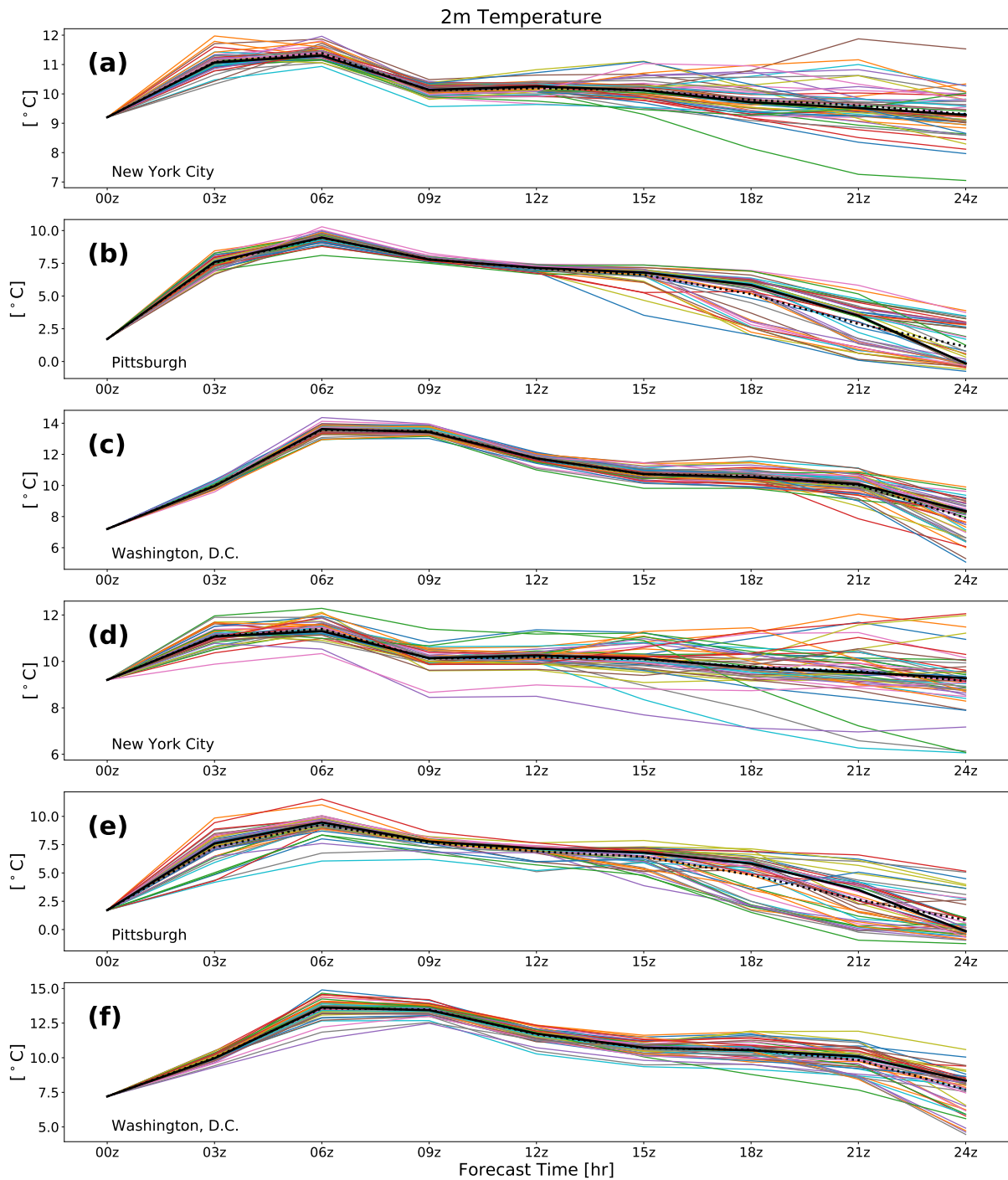


FIGURE 5.20: Plume diagram, 2m Temperatures (°C) from the WRF medium-range ensemble forecast system for EXP1 initialized at 1200 UTC 4 December 2020 for three different locations: (a) New York City, (b) Pittsburgh, and (c) Washington, D.C. Control forecast (bold black), perturb forecast (color-coded), ensemble mean (dashed black). The fields in panels (d)–(f) are repeated for EXP2.

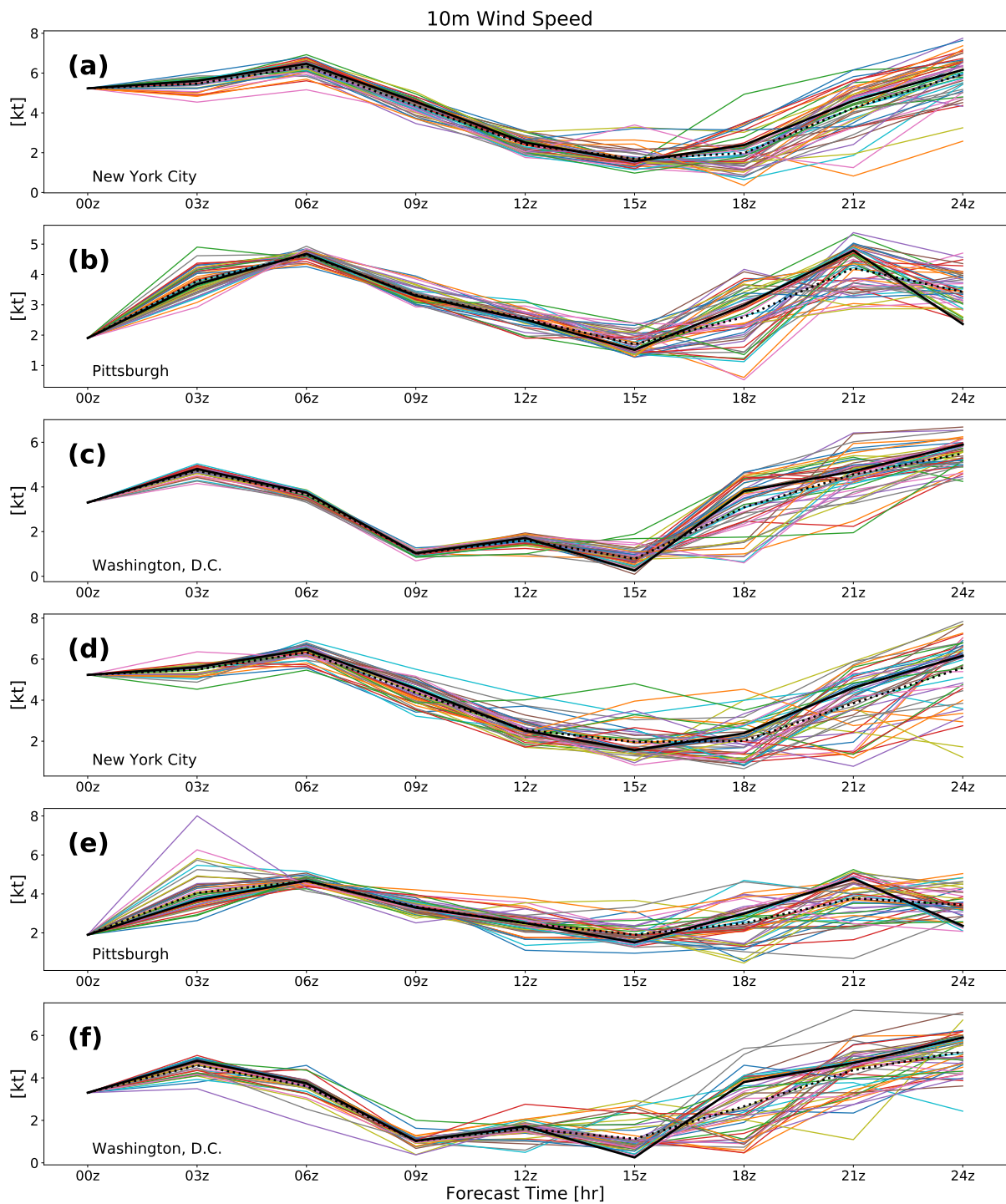


FIGURE 5.21: Plume diagram, 10m wind speed (kt) from the WRF medium-range ensemble forecast system for EXP1 initialized at 1200 UTC 4 December 2020 for three different locations: (a) New York City, (b) Pittsburgh, and (c) Washington, D.C. Control forecast (bold black), perturb forecast (color-coded), ensemble mean (dashed black).

The fields in panels (d)–(f) are repeated for EXP2.

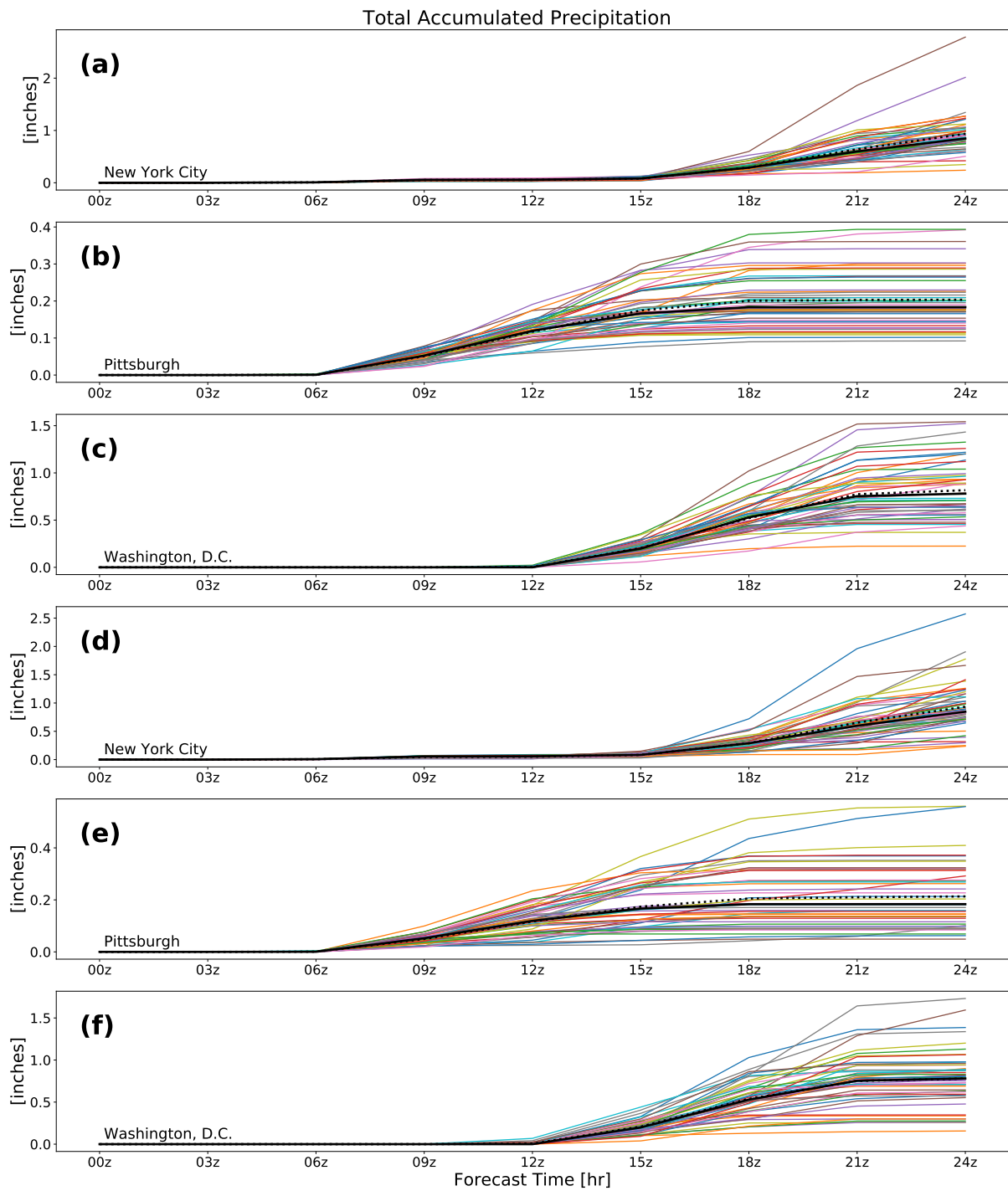


FIGURE 5.22: Plume diagram, total accumulated precipitation (inches) from the WRF medium-range ensemble forecast system for EXP1 initialized at 1200 UTC 4 December 2020 for three different locations: (a) New York City, (b) Pittsburgh, and (c) Washington, D.C. Control forecast (bold black), perturb forecast (color-coded), ensemble mean (dashed black). The fields in panels (d)–(f) are repeated for EXP2.

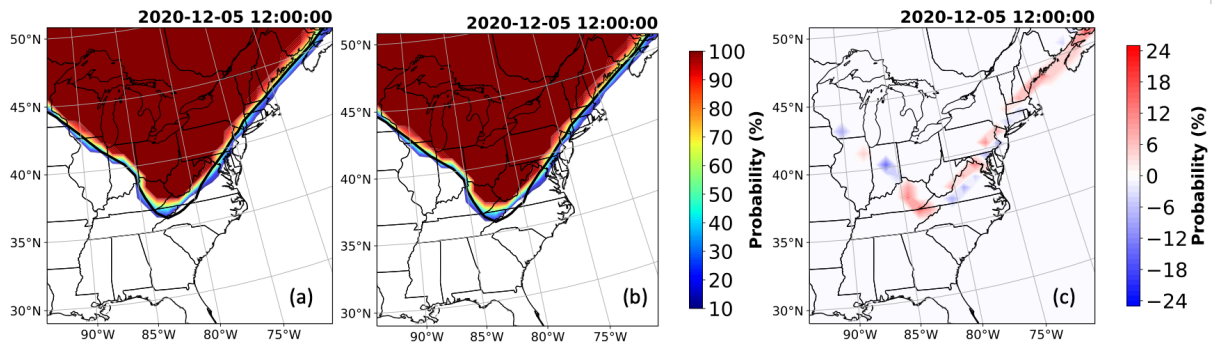


FIGURE 5.23: The probability of occurrence of this event at each grid point which computed by dividing the number of forecast members that predicted temperature below 0C by $2N+1$, the total number of forecasts for (a) EXP1, (b) EXP2 and (c) EXP1-EXP2.

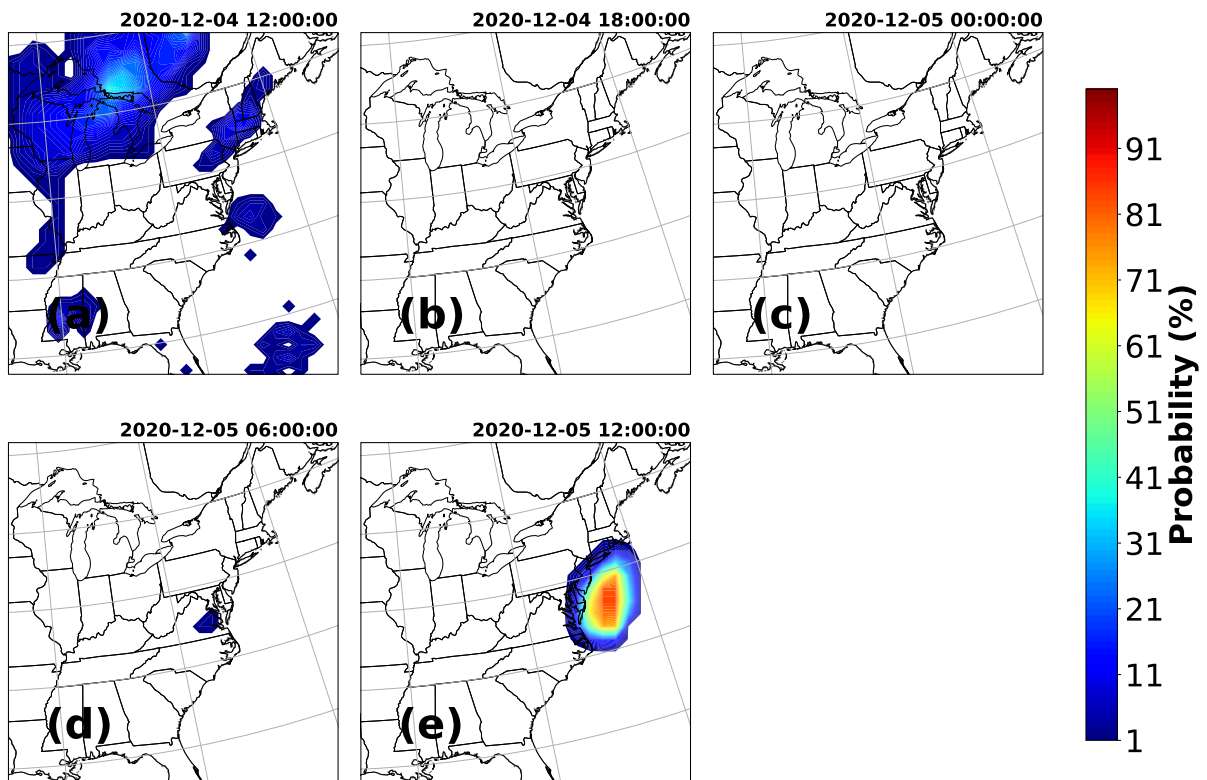


FIGURE 5.24: Forecasts of the estimated probability that SLP is below 1005 hPa during the period from 1200 UTC 4 Dec to 1200 UTC 5 Dec 2020 for EXP1.

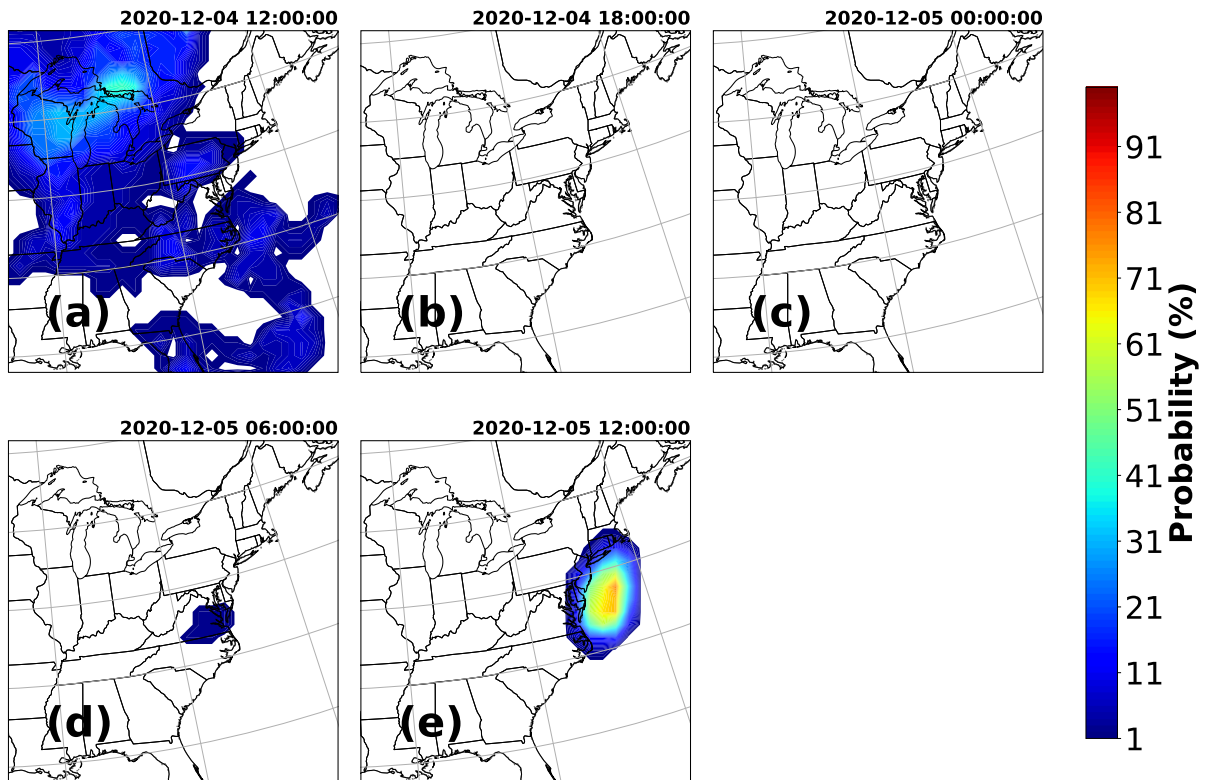


FIGURE 5.25: Forecasts of the estimated probability that SLP is below 1005 hPa during the period from 1200 UTC 4 Dec to 1200 UTC 5 Dec 2020 for EXP2.

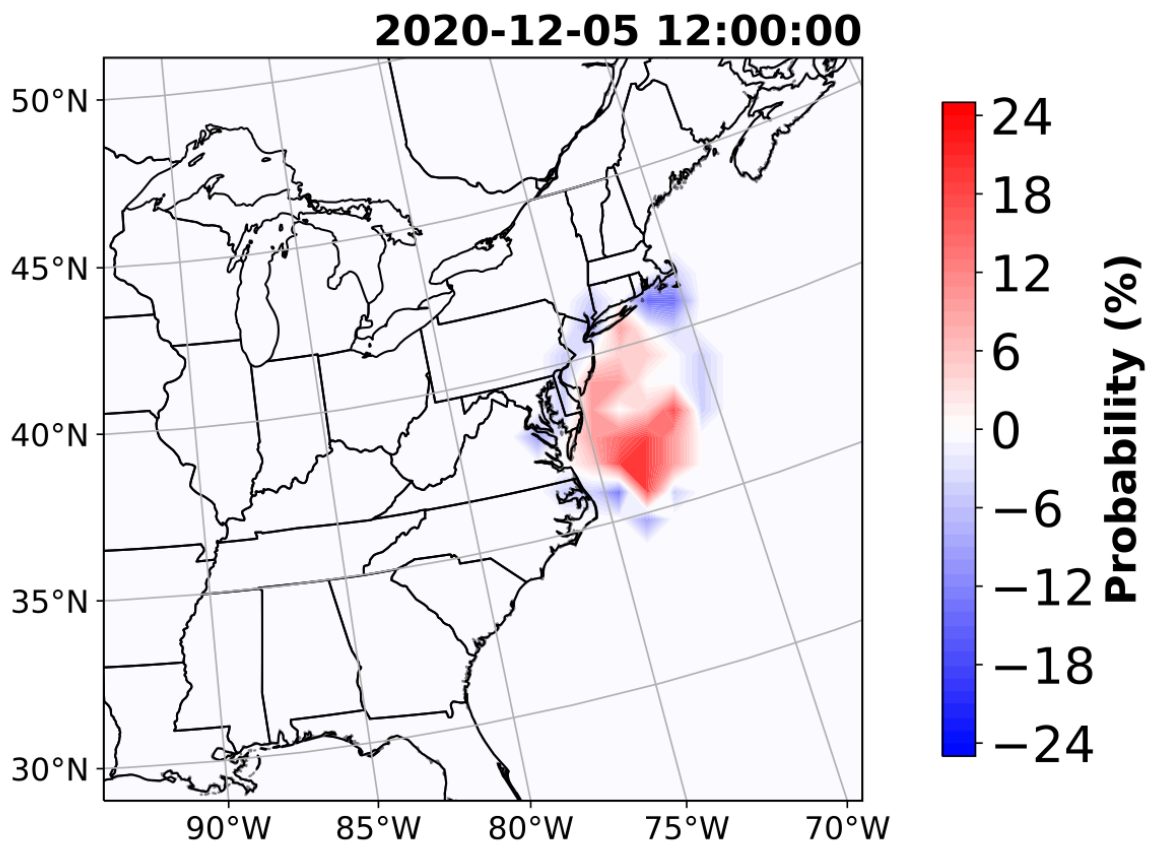


FIGURE 5.26: The difference of probability of occurrence of this event at each grid point that predicted SLP is below 1005 hPa between EXP1 and EXP2.

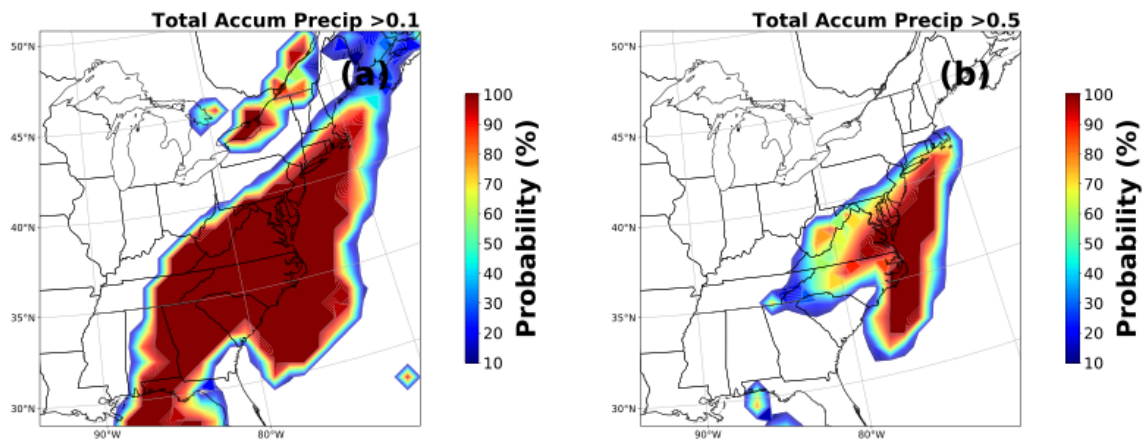


FIGURE 5.27: Forecasts of the estimated probability for different total accumulation threshold: (a) ≥ 0.1 inches, and (b) ≥ 0.5 inches at the final time 1200 UTC 5 December 2020 for EXP1.

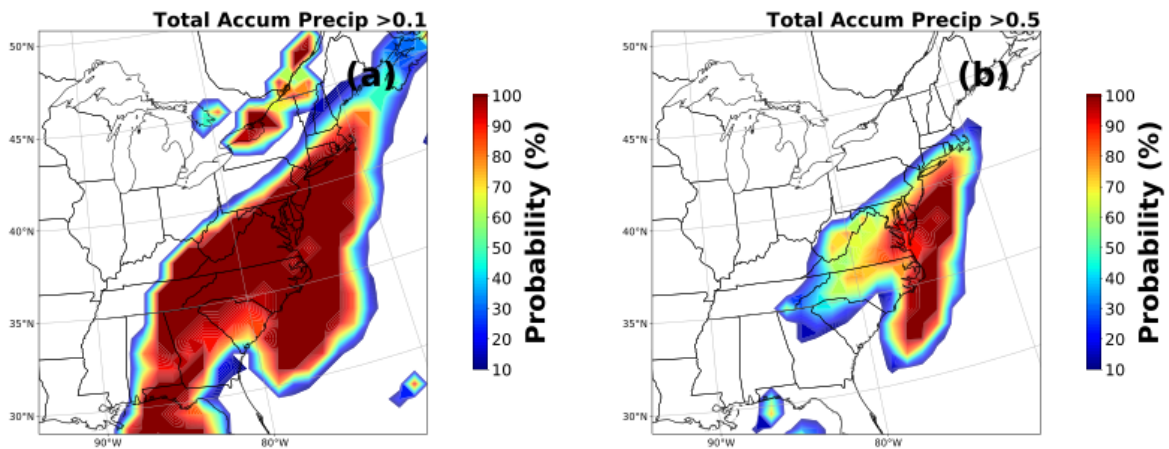


FIGURE 5.28: Forecasts of the estimated probability for different total accumulation threshold: (a) ≥ 0.1 inches, and (b) ≥ 0.5 inches at the final time 1200 UTC 5 December 2020 for EXP2.

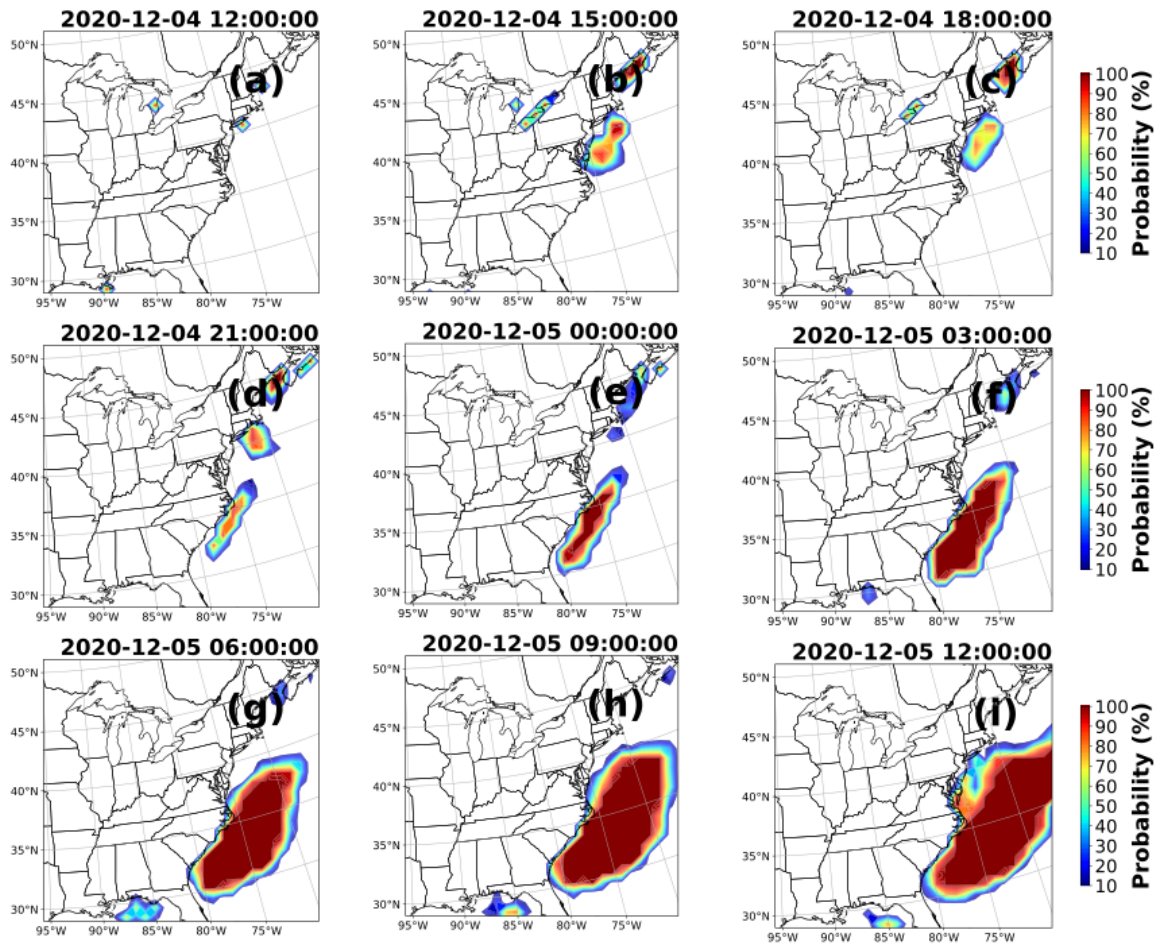


FIGURE 5.29: Forecasts of the estimated probability that wind speed at 10m is larger than 20kt during the period from 1200 UTC 4 Dec to 1200 UTC 5 Dec 2020 for EXP1.

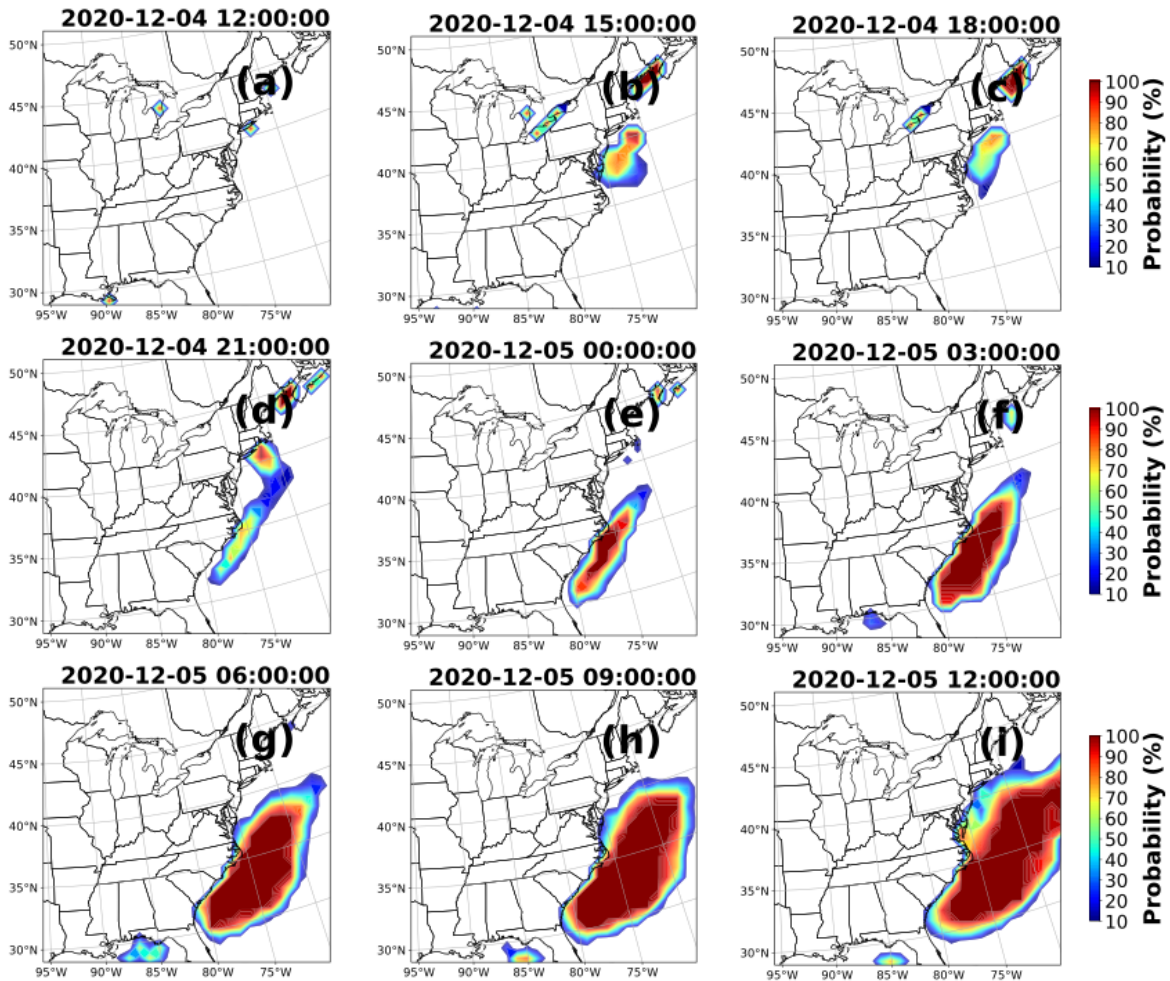


FIGURE 5.30: Forecasts of the estimated probability that wind speed at 10m is larger than 20kt during the period from 1200 UTC 4 Dec to 1200 UTC 5 Dec 2020 for EXP2.

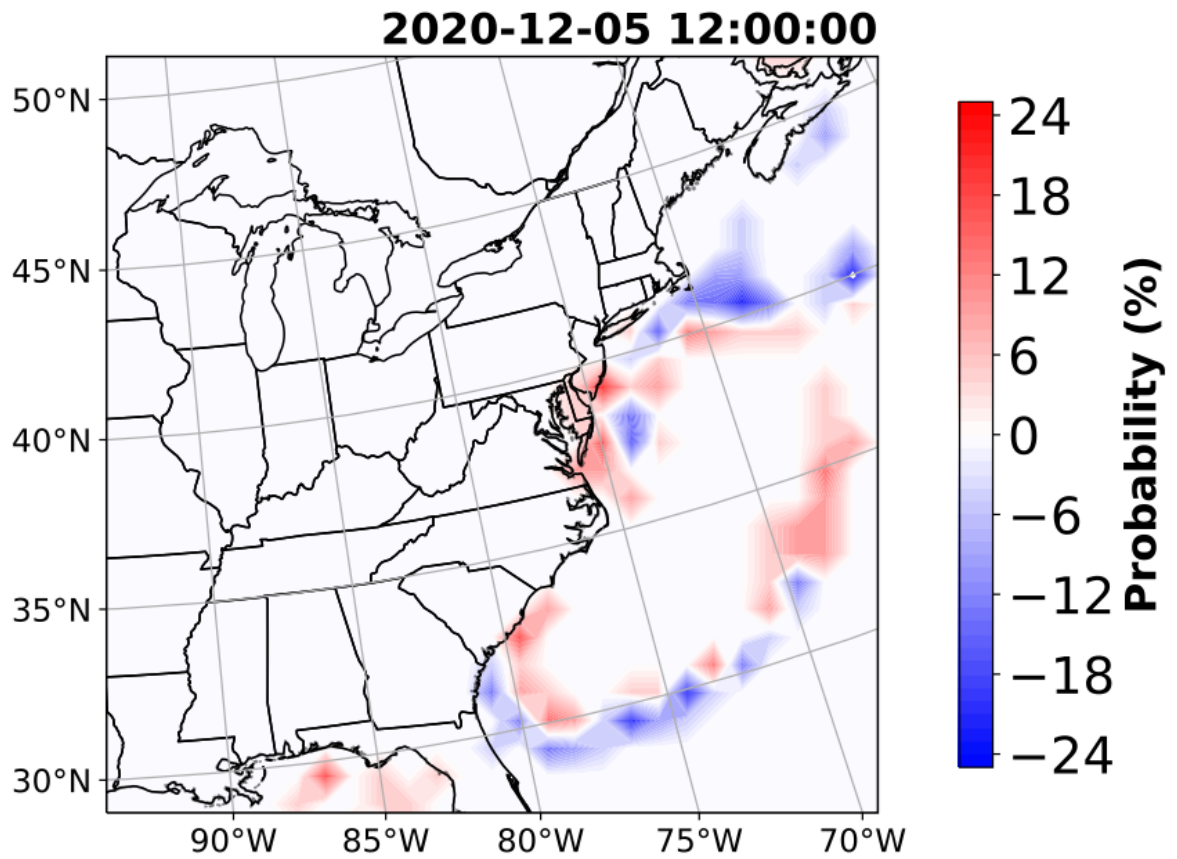


FIGURE 5.31: The difference of probability of occurrence of this event at each grid point that predicted wind speed at 10m is larger than 20 kt between EXP1 and EXP2.]

Chapter 6

Summary

The simulation of initial condition uncertainties is fundamental for creating and applying an ensemble forecast system. The preceding sections demonstrate the first-ever WRF ensemble predictions system generated using the singular vector technique for a short-range forecast. This technique was tested using a dry energy norm with a local projection operator. In addition, the initial development of ensemble post-processing methods to reveal forecast spread was demonstrated. Results from all cases analyzed (not shown), including the one presented here, are similar to previous studies (Errico and Raeder (1999); Buizza and Palmer (1995)), including the appropriateness of linearity for at least a day, the initial SV energy concentrated at lower levels, and forecast spread among variables being flow and case dependent. Initial indications show robust forecast spread for mid-latitude baroclinic systems and less spread (so far) for tropical weather systems (not shown). This may be due to the moisture variable not yet being fully incorporated

into the norm or due to the coarse resolution of the model. Although both experiments considered here reveal a spread in the forecast, as expected, incorporating an LPO over a weather feature like a mid-latitude cyclone development will concentrate perturbation growth over that feature. Therefore, it will be driving a larger spread in the development of that feature than would be achieved by SVs that are evaluated over the entire model domain. Overall, results show robust forecast spread for mid-latitude baroclinic systems and less spread for tropical weather systems (not shown). This may be due to water vapor mixing ratio not yet being incorporated into the norm or due to the coarse resolution of the model. This led to further questions such as the impact of adding the moisture term to the energy norm. This system can generate up to 11 ensemble members in two hours after 30 iterations using 40 cores on the Amazon Web Services (AWS) linux platform. This technique has been successfully implemented using AWS to benefit the operational predictions for American Family Insurance. Furthermore, experimental post-processing products have been developed to reveal the spread (i.e., standard deviation) in the model variables and estimate the probability of threshold exceedances for model variables precipitation, mean sea level pressure, and wind speed. This forecasting tool shows the uncertainty range and the most likely outcome for a weather event.

Chapter 7

Future Work

The work demonstrated in this thesis provides a platform for further exploration and development of an ensemble prediction system as well as a platform for studying the predictability of specific atmospheric phenomena. Below we discuss the immediate next steps to transform the delivered SV code to a robust operational system and some initial thoughts on how this SV code could be used to explore the predictability of organized tropical weather systems.

This work demonstrates the process and feasibility of using the WRF model, its adjoint, and its tangent linear model to calculate SVs for use as initial perturbations for an operational ensemble forecast system. The feasibility of the developed system is manifest in its being able to be successfully run at a 90km grid spacing within a time frame comparable to a 9km operational deterministic forecast with an inner grid of 3km using comparable

computing resources. In principle, the deterministic forecast, coupled with the measures of forecast spread (at coarser grid spacing) would allow forecasters to understand the flow dependent predictability for each forecast cycle. In order for this vision to be realized; however, additional work, beyond the scope of this Masters' thesis, would need to be completed. This work includes ensemble forecast calibration and verification, running the ensemble with a grid spacing commensurate with the operational deterministic system, and reconsideration of the initial and final time norms through inclusion of water vapor or through the use of an analysis error metric at the initial time.

While post-processing of the ensemble output reveals spread in the cases shown (and for others considered), an evaluation of the ensemble in terms of accuracy, skillfulness, and reliability is needed for this system to be indeed fit for operational purposes. Accuracy measures the degree of agreement between forecasts and observations, while skill is a comparative measure against a reference data set (e.g., persistence or climatology). Reliability measures how well the predicted probabilities of an event correspond to their observed frequencies. The use of the frequency of occurrence of events as a measure of probability of occurrence of those events represents a crude first step in calculating the probabilities for this system. It is proposed that application and evaluation of a probability skill score such as the Brier skill score or ranked probability skill score over an extended period, would allow quantification of the performance of the probabilistic prediction system relative to climatology. The model resolution may increase the degree of uncertainties in the forecast; hence, the nonlinear simulations to 30 km will be examined

and compared with the spread. The following step will be to create a real-time, initial ensemble prediction system for the AOS server using the WRF model.

As noted in chapter 2, the norm defining the SV amplitude at either the initial or final time has an impact on the SV structure and evolution. Previous studies (Ehrendorfer et al. (1999), Coutinho et al. (2004), Barkmeijer et al. (2001)) have shown that inclusion of water vapor perturbation energy in the initial SV norm leads to different initial structures that tend to grow faster (amplifying the forecast spread). Such perturbations are essential for SV applications in a tropical environment. Hence, test of the moist energy norm will be performed to investigate how moisture impacts the structure and evolution of WRF model SVs. Finally, it is important to note that while the energy norm has been used as a surrogate for initial time analysis uncertainty, other measures of initial time uncertainty could be considered including use of a flow-dependent, analysis error covariance (AEC) as an initial time uncertainty measure. It is recognized that the AEC is not well-characterized or calculated in contemporary data assimilation systems, but estimates of the AEC may be obtainable from ensemble Kalman filter data assimilation approaches. It would be of interest to compare SV ensembles using the dry or moist energy norms with one using an estimate for the AEC to evaluate the impact on ensemble skill and reliability.

Singular vectors identify those perturbations to a control forecast trajectory that will amplify most rapidly over a finite time, the “optimization time interval (OTI).” The growing perturbations are configured to optimally extract energy from the control trajectory’s

basic state through barotropic, baroclinic, or moist processes. The ability to identify during each forecast cycle regions for which energy is available for disturbances to develop posing an intriguing possibility - use of SVs to diagnose the development potential for atmospheric disturbances. A planned extension of this work will involve the application of SV techniques incorporating different norms to enhance the short-term development potential for African Easterly waves and tropical cyclones and the relationships between the magnitude of barotropic and baroclinic shear as well as moisture distributions to the magnitude of the singular value spectrum.

Bibliography

- Anderson, J. L., 1997: The impact of dynamical constraints on the selection of initial conditions for ensemble predictions: Low-order perfect model results. *Monthly weather review*, **125**, 2969–2983.
- Barkmeijer, R. B., J. and T. N. Palmer, 1999: 3D-Var Hessian singular vectors and their potential use in the ECMWF Ensemble Prediction System. *Quarterly Journal of the Royal Meteorological Society*, **125**, 2333–2351, doi:10.1002/qj.49712555818.
- Beare, R., A. Thorpe, and A. White, 2003: The predictability of extratropical cyclones: Nonlinear sensitivity to localized potential-vorticity perturbations. *Quarterly Journal of the Royal Meteorological Society: A journal of the atmospheric sciences, applied meteorology and physical oceanography*, **129**, 219–237.
- Bowler, N. E., 2006: Comparison of error breeding, singular vectors, random perturbations and ensemble kalman filter perturbation strategies on a simple model. *Tellus A: Dynamic Meteorology and Oceanography*, **58**, 538–548.

- Buizza, R. and T. N. Palmer, 1995: The singular-vector structure of the atmospheric global circulation. *Journal of the Atmospheric Sciences*, **52**, 1434–1456.
- Buizza, R., J. Tribbia, F. Molteni, and T. Palmer, 1993: Computation of optimal unstable structures for a numerical weather prediction model. *Tellus A*, **45**, 388–407.
- Coutinho, M., B. Hoskins, and R. Buizza, 2004: The influence of physical processes on extratropical singular vectors. *Journal of the atmospheric sciences*, **61**, 195–209.
- Descamps, L., D. Ricard, A. Joly, and P. Arbogast, 2007: Is a real cyclogenesis case explained by generalized linear baroclinic instability? *Journal of the atmospheric sciences*, **64**, 4287–4308.
- Descamps, L. and O. Talagrand, 2007: On some aspects of the definition of initial conditions for ensemble prediction. *Monthly Weather Review*, **135**, 3260–3272.
- Ehrendorfer, M., R. M. Errico, and K. D. Raeder, 1999: Singular-vector perturbation growth in a primitive equation model with moist physics. *Journal of the Atmospheric Sciences*, **56**, 1627–1648.
- Ehrendorfer, M. and J. J. Tribbia, 1997: Optimal prediction of forecast error covariances through singular vectors. *Journal of the Atmospheric Sciences*, **54**, 286–313.
- Errico, R. M. and K. D. Raeder, 1999: An examination of the accuracy of the linearization of a mesoscale model with moist physics. *Quarterly Journal of the Royal Meteorological Society*, **125**, 169–195.

- Errico, R. M., T. Vukicevic, and K. Raeder, 1993: Examination of the accuracy of a tangent linear model. *Tellus A*, **45**, 462–477.
- Farrell, B. F., 1982: The initial growth of disturbances in a baroclinic flow. *J. Atmos. Sci.*, **39**, 1663–1686.
- 1989: Optimal excitation of baroclinic waves. *Journal of Atmospheric Sciences*, **46**, 1193–1206.
- Gelaro, R., R. Buizza, T. Palmer, and E. Klinker, 1998: Sensitivity analysis of forecast errors and the construction of optimal perturbations using singular vectors. *Journal of the atmospheric sciences*, **55**, 1012–1037.
- Hakim, G. J., 2000: Role of nonmodal growth and nonlinearity in cyclogenesis initial-value problems. *Journal of the atmospheric sciences*, **57**, 2951–2967.
- Hartmann, D., R. Buizza, and T. N. Palmer, 1995: Singular vectors: The effect of spatial scale on linear growth of disturbances. *Journal of Atmospheric Sciences*, **52**, 3885–3894.
- Heideman, K. F. and J. Michael Fritsch, 1988: Forcing mechanisms and other characteristics of significant summertime precipitation. *Weather and forecasting*, **3**, 115–130.
- Hersbach, H., 2000: Decomposition of the continuous ranked probability score for ensemble prediction systems. *Weather and Forecasting*, **15**, 559–570.
- Hoskins, B. J., R. Buizza, and J. Badger, 2000: The nature of singular vector growth and structure. *Quarterly Journal of the Royal Meteorological Society*, **126**.

- Houtekamer, P. and J. Derome, 1995: Methods for ensemble prediction. *Monthly Weather Review*, **123**, 2181–2196.
- Houtekamer, P. L., L. Lefaivre, J. Derome, H. Ritchie, and H. L. Mitchell, 1996: A system simulation approach to ensemble prediction. *Monthly Weather Review*, **124**, 1225–1242.
- Houtekamer, P. L., H. L. Mitchell, G. Pellerin, M. Buehner, M. Charron, L. Spacek, and B. Hansen, 2005: Atmospheric data assimilation with an ensemble kalman filter: Results with real observations. *Monthly weather review*, **133**, 604–620.
- Kalnay, E., 2003: *Atmospheric modeling, data assimilation and predictability*. Cambridge university press.
- Kalnay, E., M. Corazza, and M. Cai, 2002: Are bred vectors the same as lyapunov vectors? *EGS general assembly conference abstracts*, 6820.
- Kim, H. M. and B.-J. Jung, 2009: Influence of moist physics and norms on singular vectors for a tropical cyclone. *Monthly weather review*, **137**, 525–543.
- Lacarra, J.-F. and O. Talagrand, 1988: Short-range evolution of small perturbations in a barotropic model. *Tellus A*, **40**, 81–95.
- Leutbecher, M., 2005: On ensemble prediction using singular vectors started from forecasts. *Monthly weather review*, **133**, 3038–3046.

- 2007: On the representation of initial uncertainties with multiple sets of singular vectors optimized for different criteria. *Quarterly Journal of the Royal Meteorological Society: A journal of the atmospheric sciences, applied meteorology and physical oceanography*, **133**, 2045–2056.
- Leutbecher, M. and T. N. Palmer, 2008: Ensemble forecasting. *Journal of computational physics*, **227**, 3515–3539.
- Lorenz, E. N., 1963: Deterministic nonperiodic flow. *Journal of atmospheric sciences*, **20**, 130–141.
- 1965: A study of the predictability of a 28-variable atmospheric model. *Tellus*, **17(3)**, 321–333, doi:10.3402/tellusa.v17i3.9076.
- Molteni, F., R. Buizza, T. N. Palmer, and T. Petroliagis, 1996: The ecmwf ensemble prediction system: Methodology and validation. *Quarterly journal of the royal meteorological society*, **122**, 73–119.
- Molteni, F. and T. Palmer, 1993: Predictability and finite-time instability of the northern winter circulation. *Quarterly Journal of the Royal Meteorological Society*, **119**, 269–298.
- Montani, A. and A. J. Thorpe, 2002: Mechanisms leading to singular-vector growth for FASTEX cyclones. *Quarterly Journal of the Royal Meteorological Society*, **128**, 131–148, doi:10.1256/00359000260498824.

- Morgan, M. C., 1999: Using piecewise potential vorticity inversion to diagnose frontogenesis. part i: A partitioning of the q vector applied to diagnosing surface frontogenesis and vertical motion. *Monthly weather review*, **127**, 2796–2821.
- Mukougawa, H. and T. Ikeda, 1994: Optimal excitation of baroclinic waves in the eady model. *Journal of the Meteorological Society of Japan. Ser. II*, **72**, 499–513.
- Palmer, T., R. Gelaro, J. Barkmeijer, and R. Buizza, 1998a: Singular vectors, metrics, and adaptive observations. *Journal of the Atmospheric Sciences*, **55**, 633–653.
- 1998b: Singular vectors, metrics, and adaptive observations. *Journal of the Atmospheric Sciences*, **55**, 633–653.
- Palmer, T. N., 1993: Extended-range atmospheric prediction and the lorenz model. *Bulletin of the American Meteorological Society*, **74**, 49–66.
- Palmer, T. N., R. Buizza, F. Molteni, Y.-Q. Chen, and S. Corti, 1994: Singular vectors and the predictability of weather and climate. *Philosophical Transactions of the Royal Society of London. Series A: Physical and Engineering Sciences*, **348**, 459–475.
- Parlett, B. N., 1980: A new look at the lanczos algorithm for solving symmetric systems of linear equations. *Linear algebra and its applications*, **29**, 323–346.
- Powers, J. G., J. B. Klemp, W. C. Skamarock, C. A. Davis, J. Dudhia, D. O. Gill, J. L. Coen, D. J. Gochis, R. Ahmadov, S. E. Peckham, et al., 2017: The weather research and forecasting model: Overview, system efforts, and future directions. *Bulletin of the American Meteorological Society*, **98**, 1717–1737.

- Skamarock, W. C., J. B. Klemp, J. Dudhia, D. O. Gill, D. M. Barker, W. Wang, and J. G. Powers, 2008: A description of the advanced research wrf version 3. ncar technical note -475+str.
- Stensrud, D. J., H. E. Brooks, J. Du, M. S. Tracton, and E. Rogers, 1999: Using ensembles for short-range forecasting. *Monthly Weather Review*, **127**, 433–446.
- Toth, Z. and E. Kalnay, 1993: Ensemble forecasting at nmc: The generation of perturbations. *Bulletin of the american meteorological society*, **74**, 2317–2330.
- Trevisan, A. and R. Legnani, 1995: Transient error growth and local predictability: A study in the lorenz system. *Tellus A*, **47**, 103–117.
- Wei, M. and J. Frederiksen, 2004: Error growth and dynamical vectors during southern hemisphere blocking. *Nonlinear Processes in Geophysics*, **11**, 99–118.
- Wei, M., Z. Toth, R. Wobus, and Y. Zhu, 2008: Initial perturbations based on the ensemble transform (et) technique in the ncep global operational forecast system. *Tellus A: Dynamic Meteorology and Oceanography*, **60**, 62–79.
- Wei, M., Z. Toth, R. Wobus, Y. Zhu, C. H. Bishop, and X. Wang, 2006: Ensemble transform kalman filter-based ensemble perturbations in an operational global prediction system at ncep. *Tellus A: Dynamic Meteorology and Oceanography*, **58**, 28–44.
- Yang, S.-C., E. Kalnay, and T. Enomoto, 2015: Ensemble singular vectors and their use as additive inflation in enkf. *Tellus A: Dynamic Meteorology and Oceanography*, **67**, 26536.

Zhou, X., Y. Zhu, D. Hou, and D. Kleist, 2016: A comparison of perturbations from an ensemble transform and an ensemble kalman filter for the ncep global ensemble forecast system. *Weather and Forecasting*, **31**, 2057–2074.